

See discussions, stats, and author profiles for this publication at: <https://www.researchgate.net/publication/235657518>

Tunable Plasmonic Coupling in Self-Assembled Binary Nanocrystal Super lattices Studied by Correlated Optical Microspectrophotometry and Electron Microscopy

ARTICLE *in* NANO LETTERS · FEBRUARY 2013

Impact Factor: 13.59 · DOI: 10.1021/nl400052w · Source: PubMed

CITATIONS

29

READS

86

4 AUTHORS, INCLUDING:



Xingchen Ye

University of California, Berkeley

57 PUBLICATIONS 2,753 CITATIONS

[SEE PROFILE](#)



Christopher B Murray

University of Pennsylvania

259 PUBLICATIONS 27,426 CITATIONS

[SEE PROFILE](#)

Tunable Plasmonic Coupling in Self-Assembled Binary Nanocrystal Superlattices Studied by Correlated Optical Microspectrophotometry and Electron Microscopy

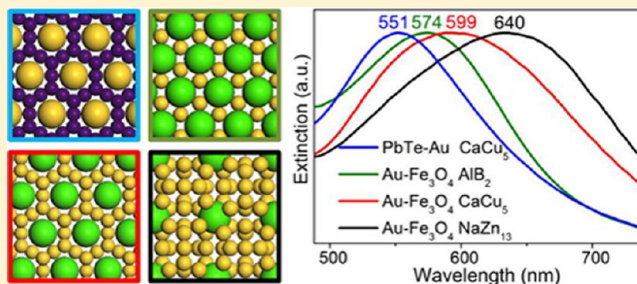
Xingchen Ye,[†] Jun Chen,[†] Benjamin T. Diroll,[†] and Christopher B. Murray*,^{*,†,‡}

[†]Department of Chemistry and [‡]Department of Materials Science and Engineering, University of Pennsylvania, Pennsylvania 19104, United States

Supporting Information

ABSTRACT: We study the plasmonic properties of self-assembled binary nanocrystal superlattices (BNSLs) using correlated optical microspectrophotometry and electron microscopy performed on individual BNSL domains. The strength of near-field couplings between adjacent plasmonic nanocrystals (NCs) can be systematically engineered by varying the NC size, composition, and the lattice symmetry of BNSLs, leading to broadband spectral tunability of the collective plasmonic response of BNSLs across the entire visible spectrum. Self-assembled multicomponent NC superlattices represent a versatile platform for the rational design of macroscopic three-dimensional plasmonic metamaterials with emergent optical characteristics.

KEYWORDS: *Self-assembly, binary nanocrystal superlattices, collective plasmonic response, near-field coupling, microspectrophotometry, surface plasmon resonance*



The vivid color change when a dilute solution of Au nanocrystals (NCs) aggregates has captured the imagination of scientists from many disciplines.^{1–6} This color change and the dramatic enhancement of local electromagnetic fields within metal NC aggregates have enabled a variety of new technologies including surface-enhanced spectroscopies,^{7,8} plasmonic sensors,^{1,9} and plasmonic rulers.^{10,11} Recently, clusters composed of densely packed plasmonic NCs have been demonstrated to support intriguing new phenomena such as magnetic resonances, Fano resonances arising from the interference between electric and magnetic plasmonic modes, and so forth.^{12–15} Significant progress has been achieved over the past decade on the fabrication of plasmonic nanoparticle clusters, chains, and two-dimensional arrays using top-down lithographic and patterning techniques.^{6,11,16–18} However, the polycrystalline nature of metallic nanostructures created by these methods often leads to damping of surface plasmons due to scattering at internal defects, grain boundaries, or surface roughness and decrease in the quality factor of surface plasmon resonance (SPR). Furthermore, it is extremely difficult to fabricate strongly coupled plasmonic nanostructures with very small interparticle separations (<5 nm).

Alternatively, chemical synthesis of plasmonic NCs with well-tailored sizes, compositions, morphologies, and optical signatures and bottom-up assembly into NC superlattices provide a programmable approach to design NC-based plasmonic metamaterials with customized optical properties.^{12,19–30} For example, Tao et al. demonstrated assembly of polyhedral Ag NCs into two-dimensional (2D) plasmonic

superlattices using the Langmuir–Blodgett method.²¹ Chen et al. prepared 2D hexagonal close-packed (hcp) superlattices of 10.5 nm Au NCs and showed that by decreasing the length of thiolate ligands, the plasmon resonance shifts toward lower energies as a result of increasing near-field coupling between neighboring NCs.²² Despite these advances on 2D plasmonic NC superlattices, controlled assembly of large-scale three-dimensional (3D) plasmonic NC oligomers or clusters with well-defined spatial regularity and desired groupings of NCs has been a long-standing challenge. Molecular assembly strategies such as the use of DNA linkers have been shown to be effective for constructing complex 2D and 3D plasmonic NC clusters.^{26,27,31,32} However, the requirement to achieve precise cluster geometries and more importantly, to realize small interparticle distances that provide strong plasmonic couplings in some cases contrasts the current capabilities with DNA-based design. Binary nanocrystal superlattices (BNSLs) in which two types of NCs are coassembled into ordered arrays have received significant attention in recent years. Compared to single-component NC superlattices, complex interparticle interactions present in BNSLs can lead to collective physical properties that are distinct from simply the sum of those of the two NC constituents.^{33–42} While relatively unexplored, BNSLs also provide a versatile platform for bottom-up design of NC-

Received: January 6, 2013

Revised: February 14, 2013

Published: February 18, 2013

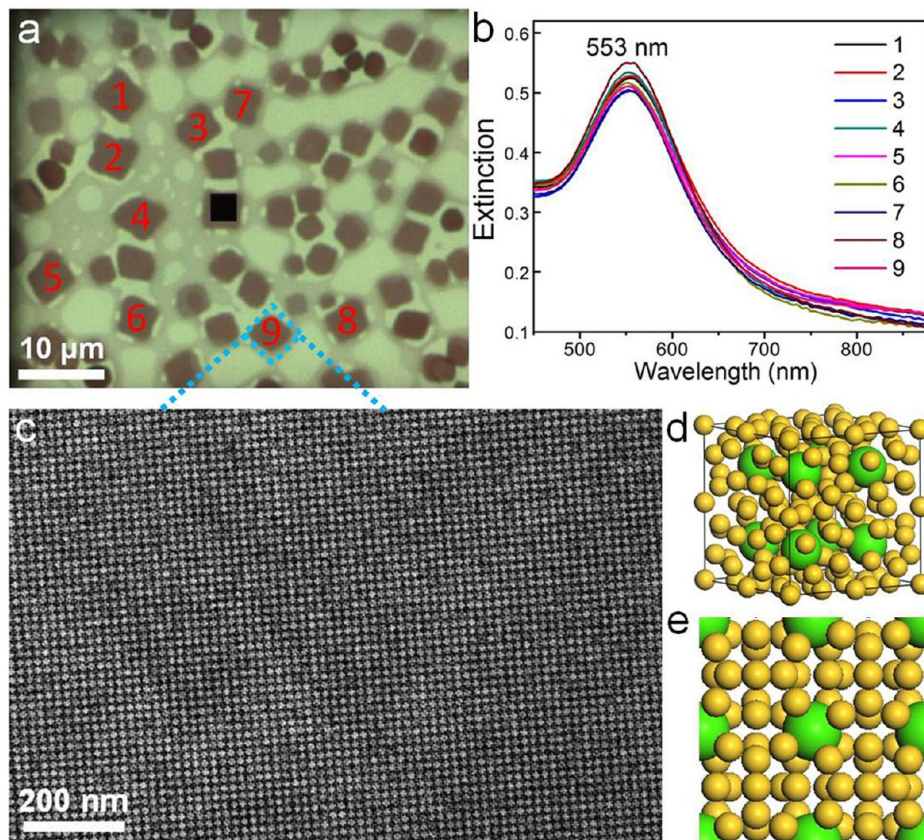


Figure 1. (a) Representative optical micrograph of NaZn₁₃-type BNSLs self-assembled from 5.5 nm DDT-stabilized Au NCs and 9.6 nm Fe₃O₄ NCs. (b) Extinction spectra collected from different single-crystalline BNSL domains as labeled in the corresponding optical micrographs. A 100× objective lens is used and the optical sampling area is 3.1 μm × 3.1 μm. (c) TEM image of [001]-oriented NaZn₁₃-type BNSLs from self-assembled 5.5 nm DDT-stabilized Au NCs and 9.6 nm Fe₃O₄ NCs. Structural models of (d) the unit cell and (e) the [001] projection of NaZn₁₃-type BNSLs.

based plasmonic metamaterials, as the strength of near-field couplings between adjacent plasmonic NCs can be systematically engineered by varying the NC size, composition and the lattice symmetry of BNSLs.

In this contribution, we demonstrate for the first time, tunable collective plasmonic response in BNSLs self-assembled from plasmonic (Ag, Au) and nonplasmonic (Fe₃O₄, PbS, PbTe) NCs. A rich array of BNSL phases are accessed by using an interfacial assembly approach.^{37,43} In a typical process, a colloidal solution of two different types of NCs is spread onto an immiscible glycolic liquid subphase, forming immediately a thin wetting layer. Upon drying of the NC solvent, the fluid-supported BNSL films can be transferred onto optically transparent substrates such as carbon-coated TEM grids used in this study. An optical micrograph of BNSL films is shown in Figure 1a. Each faceted domain in the image represents a BNSL crystallite grain. In contrast, the lighter regions are usually sparsely covered by NCs (i.e., not BNSLs). It is important to point out that in this work the more polar liquid subphase—ethylene glycol (EG) is employed for BNSL formation instead of diethylene glycol (DEG) used in previous reports. While DEG tends to produce continuous membranes consisting of a mosaic of BNSL domains with different growth directions,^{37,40} EG tends to favor semicontinuous or discontinuous films composed of isolated BNSL domains. We have exploited the discrete single-crystalline superlattice grains formed on an EG subphase for correlated optical and electron microscopy studies of BNSLs. A microspectrophotometry setup is used to probe, one domain at a time, the plasmonic properties of BNSLs,

which are very difficult to obtain using ensemble spectroscopic techniques. Because of the diffraction-limited spatial resolution of optical microscopy, individual BNSL domains to be studied optically are also imaged by TEM to establish accurate and reliable structure–property relationships. Practically, identification of exactly the same BNSL domain between optical and TEM images is achieved by taking low-magnification TEM images of neighboring meshes as well as unique morphological features of the BNSL films, which is sufficient for locating the same area under optical microscopes. We stress that low-dose electron beam irradiation is adopted during TEM characterization of NC superlattices in order to prevent possible fusion or coalescence of metal NCs.

The example shown in Figure 1 is NaZn₁₃-type BNSLs self-assembled from 5.5 nm dodecanethiol (DDT)-stabilized Au NCs and 9.6 nm Fe₃O₄ NCs. The unit cell of the NaZn₁₃ (space group $Fm\bar{3}c$) phase (Figure 1d) consists of 104 small spheres and 8 large spheres.⁴⁴ The structure can be viewed in the following manner: inside a simple cubic lattice of large spheres is an icosahedron formed by 13 small spheres. The orientation of neighboring icosahedra is rotated by 90°. Figure 1c shows a TEM image of the [001]-oriented BNSL domain as indicated in Figure 1a. The cubic symmetry of the NaZn₁₃ structure is also vividly manifested by the square-like morphology of BNSL crystallites seen in the optical micrograph (Figure 1a). The lateral dimensions of individual BNSL domains are on the order of several micrometers, and the smallest optical sampling area (as indicated by the black square in Figure 1a) of the microspectrophotometry measurement

setup is about $3.1 \mu\text{m} \times 3.1 \mu\text{m}$. The collective plasmonic response of the NaZn_{13} -type BNSLs shows a single resonance peak centered at about 553 nm (Figure 1b). Excellent spectral reproducibility is obtained at multiple BNSL domains (Figure 1b). Moreover, the magnitude of extinction can be used as a measure of the relative thickness among different areas of BNSL films.

The extinction spectrum of isolated 5.5 nm Au NCs dispersed in hexane shows an SPR peak around 516 nm (Figure 2c), which is the origin of the well-known ruby-red

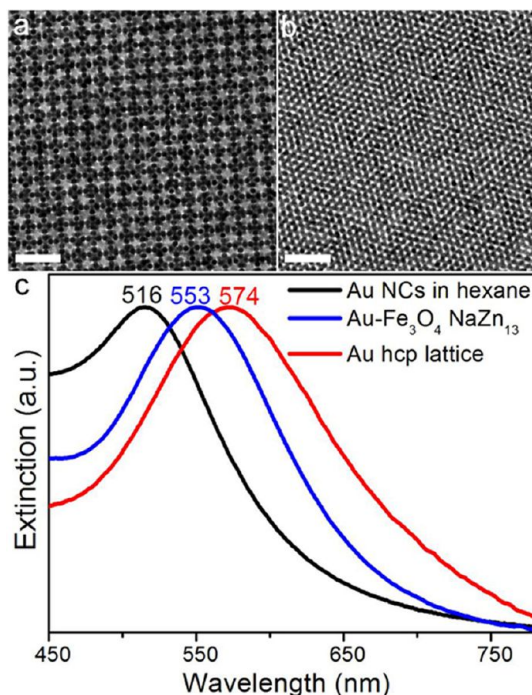


Figure 2. (a) TEM image of NaZn_{13} -type BNSLs self-assembled from 5.5 nm DDT-stabilized Au NCs and 9.6 nm Fe_3O_4 NCs. (b) TEM image of hcp superlattices (three layers thick) of 5.5 nm DDT-stabilized Au NCs. (c) Representative normalized extinction spectra collected from a hexane solution of 5.5 nm DDT-stabilized Au NCs (black curve), a single domain of NaZn_{13} -type BNSLs self-assembled 5.5 nm DDT-stabilized Au NCs and 9.6 nm Fe_3O_4 NCs (blue curve, $3.1 \mu\text{m} \times 3.1 \mu\text{m}$ sampling area), and a single hcp superlattice domain (three layers thick) of 5.5 nm DDT-stabilized Au NCs (red curve, $5.3 \mu\text{m} \times 5.3 \mu\text{m}$ sampling area). The scale bars in (a) and (b) represent 50 nm.

color of small gold colloids. When thirteen 5.5 nm Au NCs start to pack and form icosahedral clusters as in the case of NaZn_{13} -type BNSLs, a pronounced red shift (37 nm) of the extinction peak is observed (Figure 2c). The SPR band is further broadened and red shifted to 574 nm for hexagonal close-packed (hcp) superlattices (three layers thick, the ABA packing) of 5.5 nm Au NCs (Figure 2c and Supporting Information Figures S1–S3). The spectral shifts are strong indication of interparticle electromagnetic couplings in metal NC assemblies.^{6,19} Because of the relatively small NC size, both long-range radiative coupling and multipolar interactions are negligible. On the other hand, near-field coupling can play an important role for these nearly touching, deeply subwavelength metal NCs and is expected to dictate the collective plasmonic response.^{6,21,22,45} Since the evanescent near-field decays exponentially with increasing distance from the NC surface,

interparticle distances can dramatically affect the strength of plasmonic near-field coupling.^{6,22} Although it is extremely challenging to experimentally determine the nearest-neighbor gap sizes between metal NCs in many 3D BNSL structures due to the similar close-packed nature, a good estimation can be achieved by calculating the average interparticle distance along the [100] direction (the close-packed direction) from TEM images of single-component hcp NC superlattices. For DDT-capped Au and Ag NCs, the interparticle separation is measured to be about 1.5 nm (Supporting Information Figures S2 and S22), and is about 1.7 nm for oleylamine-passivated 9.7 nm Au NCs (Supporting Information Figure S6). For 5.5 nm Au NCs, the 1.5 nm gap size is around the upper limit for effective near-field plasmonic coupling predicted for noble metal NC pairs.⁶ Moreover, the difference in SPR wavelengths between NaZn_{13} -type BNSLs and hcp superlattices of Au NCs can be understood by a larger average number of nearest-neighboring NCs in the latter structure.⁴⁶

To further increase the strength of plasmonic coupling through near-field interactions and to expand the spectral range of collective plasmonic resonance in NC assemblies, larger Au NCs (9.7 nm in diameter) are employed for superlattice formation. As shown in Figure 3, hcp superlattices (three layers

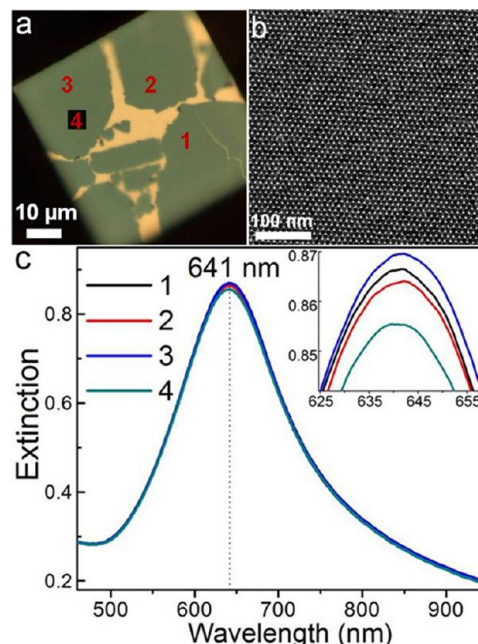


Figure 3. (a) Representative optical micrograph and (b) TEM image of self-assembled hcp superlattices of 9.7 nm oleylamine-stabilized Au NCs. (c) Extinction spectra collected from different superlattice domains as labeled in (a). Inset of (c) is a magnified view of the spectra around LSPL peaks. A 50× objective lens is used and the optical sampling area is $5.3 \mu\text{m} \times 5.3 \mu\text{m}$.

thick) of 9.7 nm Au NCs exhibit a dominant plasmonic peak centered at about 641 nm, a 123 nm red shift from the SPR wavelength of NCs dispersed in hexane (518 nm). Compared to the 58 nm red shift observed in the case of 5.5 nm Au NC superlattices (Figure 2c), this suggests a greater plasmonic coupling with increasing NC sizes given similar lattice symmetries and interparticle spacings. Furthermore, a blue shift (as large as 12 nm) in the resonance energy of hcp superlattices is consistently observed as the number of NC layers increases (Supporting Information Figures S6–S8). This

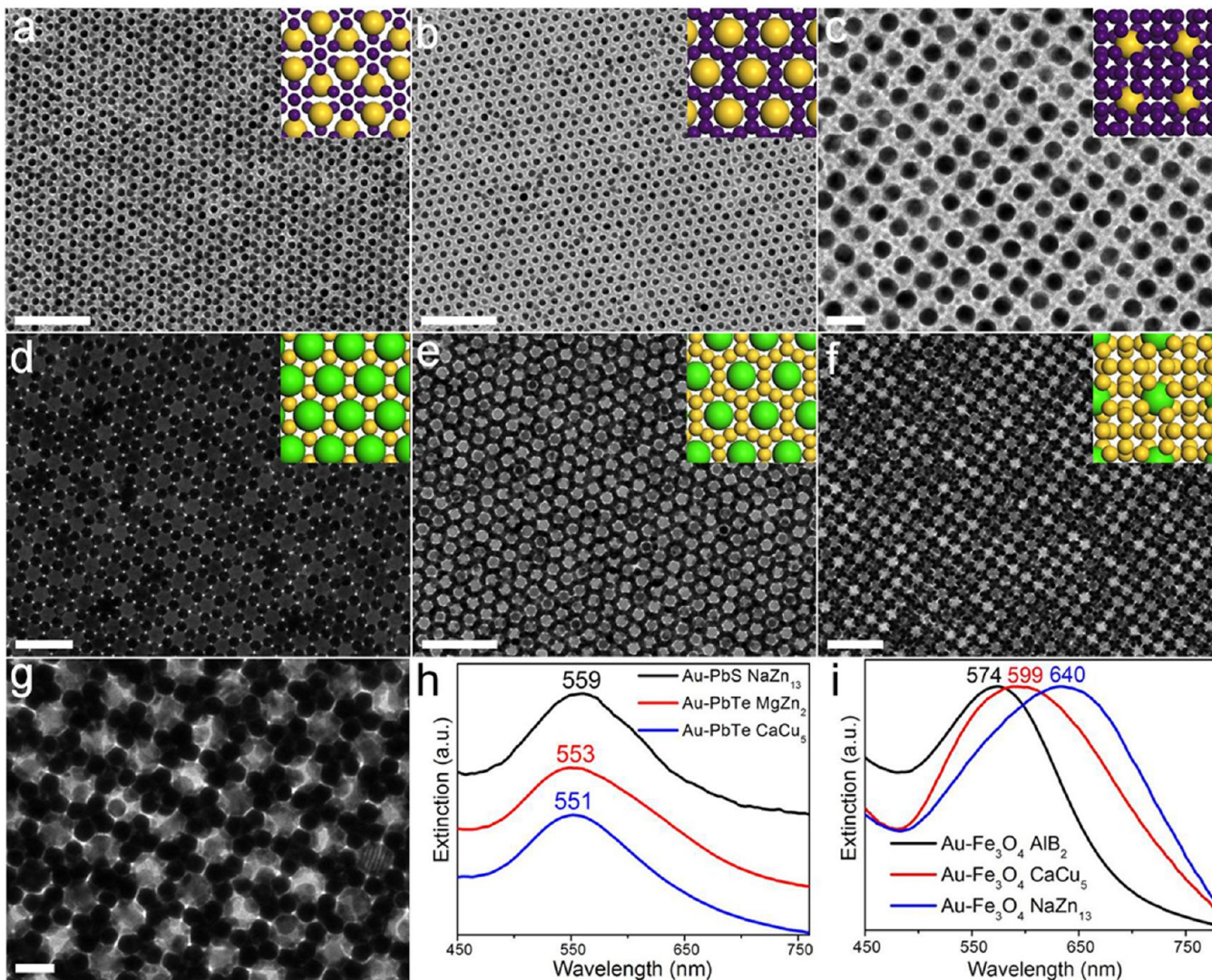


Figure 4. TEM images of (a) MgZn₂-type and (b) CaCu₅-type BNSLs self-assembled from 9.7 nm oleyamine-stabilized Au NCs and 5.8 nm PbTe NCs. (c) TEM image of NaZn₁₃-type BNSLs self-assembled from 9.7 nm oleyamine-stabilized Au NCs and 3.8 nm PbS NCs. TEM images of (d) AlB₂-type and (f,g) NaZn₁₃-type BNSLs self-assembled from 9.7 nm oleyamine-stabilized Au NCs and 17.1 nm Fe₃O₄ NCs. (e) TEM image of CaCu₅-type BNSLs self-assembled from 9.7 nm oleyamine-stabilized Au NCs and 14.1 nm Fe₃O₄ NCs. Insets of (a–f) are structural models of corresponding projections of BNSLs. (h) Representative normalized extinction spectra taken from a single domain of BNSLs shown in (a–c). Spectra have been offset vertically for clarity. (i) Representative normalized extinction spectra taken from a single domain of BNSLs shown in (d–g). The optical sampling area is 5.3 $\mu\text{m} \times 5.3 \mu\text{m}$ for BNSLs shown in (b) and (d) and is 3.1 $\mu\text{m} \times 3.1 \mu\text{m}$ for BNSLs shown in (a), (c), and (e–g). Scale bars: (a,b,e,f) 100 nm, (d) 50 nm, and (c,g) 20 nm.

phenomenon can be accounted for by the phase-retarded higher order modes arising from couplings between different NC layers, as proposed in a recent theoretical work on plasmonic nanoparticle superlattices.¹⁵ The slight shift of SPR toward higher energy with increasing sample thickness is also observed for superlattices of smaller-sized Au NCs (Supporting Information Figure S1) and BNSLs (Supporting Information Figures S4, S16). However, this contribution is typically much smaller (a few nanometers) than the spectral shifts induced by changes in lattice symmetry or arrangements of metal NCs in BNSLs.

The availability of monodisperse 9.7 nm Au NCs allows for the creation of a wide variety of plasmonic BNSL structures. Six distinct BNSL phases with domain sizes exceeding 10 μm^2 are shown in Figure 4. By varying the NC size ratio and NC concentration ratio in the spreading solutions, MgZn₂-, CaCu₅- and NaZn₁₃-type BNSLs in which Au NCs are the larger NC

constituent can be obtained (Figure 4a–c and Supporting Information Figures S9–S14). In all three structures, adjacent Au NCs are separated from each other by at least 5 nm due to the presence of rings or clusters composed of several smaller PbS or PbTe NCs. Therefore, they can be regarded as solid solutions of isolated Au NCs, and near-field couplings between Au NCs are not expected. As shown in Figure 4h, the optical extinction spectra of these BNSLs display a single SPR peak between 550 and 560 nm. The spectral red shifts compared to the SPR wavelength (518 nm) of Au NCs dispersed in hexane can be explained by variations in local dielectric environment of Au NCs. More dramatic changes in plasmon resonance are observed in BNSL structures where Au NCs are the smaller NC components. Figure 4d–g shows three different BNSL phases self-assembled from 9.7 nm Au NCs and larger Fe₃O₄ NCs. In the AlB₂-type structure, Au NCs arrange into a Kagome-type hexagonal layer alternating with layers of Fe₃O₄

NCs. The plasmonic resonance of the AlB_2 structure peaks at about 574 nm (Figure 4i and Supporting Information Figures S15–S16), and the lower resonance energy compared to BNSLs shown in Figure 4a–c is consistent with a smaller average nearest-neighbor interparticle spacing of about 2.7 nm determined from high-magnification TEM images (Supporting Information Figure S17). The dominant extinction peak further red shifts and becomes substantially broadened in CaCu_5 - and NaZn_{13} -type BNSLs (Figure 4i and Supporting Information Figures S18–21). The CaCu_5 structure can be described as a simple hexagonal lattice of large NCs surrounded by a hexagonal arrangement of small NCs occupying the trigonal prismatic interstices of the basal planes.⁴⁶ An additional layer of small NCs organized into a Kagome-type lattice exist between the basal planes. The most intriguing structural feature of the CaCu_5 phase is the extended network of interconnected rings comprised of small NCs, which makes it distinct from phases such as CaB_6 or NaZn_{13} where small NCs form well-defined isolated clusters (octahedral and icosahedral clusters, respectively) embedded in the simple cubic lattice of large NCs.^{41,44} The continuous sublattice of small metal NCs in CaCu_5 structure might be able to support propagating surface plasmons upon increasing the electronic couplings between adjacent NCs.⁴⁷ Furthermore, the difference in SPR wavelengths between CaCu_5 and NaZn_{13} BNSLs arises mainly from dissimilar local packings of Au NCs. Since both structures are densely packed NC arrays, the spacings between metal NCs in close mutual proximity are limited by the thickness of the organic stabilizer shell. However, the average coordination number (or the number of nearest neighbors) of small metal NCs is higher in the NaZn_{13} structure than the CaCu_5 structure,⁴⁶ and therefore energetically favorable near-field couplings lead to a lower energy resonance. It is clear that near-field interactions affect the frequency and the strength of plasmon resonance of BNSLs in a manner more complicated than noble metal NC pairs, and an accurate prediction of the optical properties of BNSLs having well-defined internal arrangements of plasmonic NCs is underway.

We extend the design space of plasmonic BNSLs through incorporation of Ag NCs. Among the common coinage metals, Ag is often more desirable than Au and Cu for plasmonic and metamaterial applications because of its sharper resonance, greater electromagnetic field enhancement and lower loss.^{23,24} Here we have developed a novel microwave-assisted synthesis of monodisperse spherical Ag NCs (see Methods in the Supporting Information for full detail). Upon ligand-exchange with DDT molecules, SPR of Ag NCs measured by ensemble extinction spectroscopy red shifts from 417 to 422 nm and broadens (Figure 5h), which is consistent with previous reports of chemical interface damping in small metal NCs induced by thiol groups.^{23,48,49} Using 5.4 nm Ag and 9.3 nm PbS NCs as the building blocks, both CsCl- and AlB_2 -type BNSLs can be obtained by adjusting the relative concentration between large and small NCs. In the CsCl structure, individual Ag NCs are isolated from each other by about 11 nm due to the presence of PbS NC spacers so that near-field couplings between Ag NCs are strongly suppressed (Figure 5a). Therefore, the SPR of CsCl-type BNSLs occurs at slightly lower energy (438 nm) than that of Ag NC solutions (422 nm) due to the change in dielectric constants of the medium (Figure 5i and Supporting Information Figure S24). Further spectral red shifts are observed when Ag NCs are allowed to group together in a well-defined manner (Figure 5i). The AlB_2 structure features an

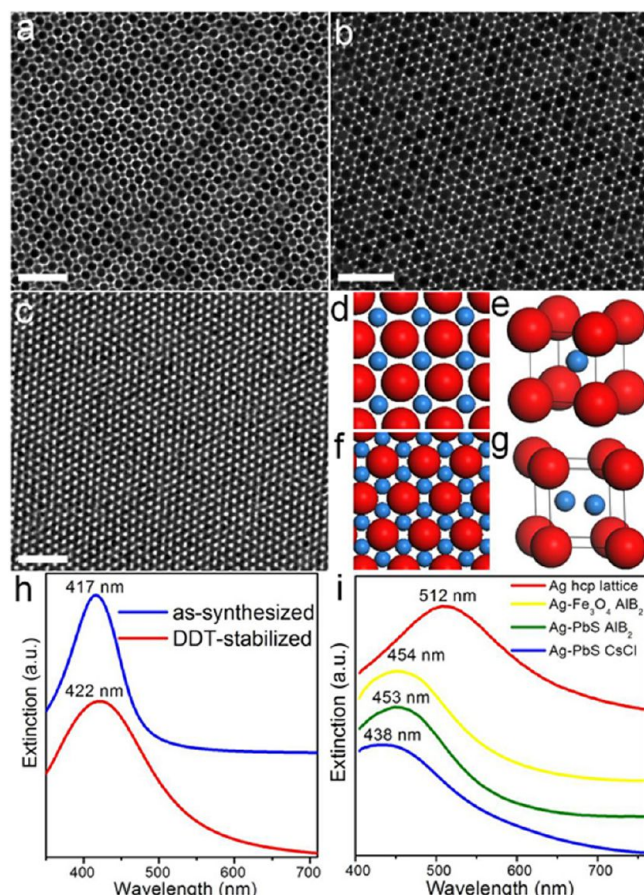


Figure 5. TEM images of (a) CsCl-type and (b) AlB_2 -type BNSLs self-assembled from 5.4 nm DDT-stabilized Ag NCs and 9.3 nm PbS NCs. (c) TEM image of hcp superlattices (three layers thick) of 5.4 nm DDT-stabilized Ag NCs. Structural models of (d) the [001] projection and (e) the unit cell of CsCl-type BNSLs. Structural models of (f) the [001] projection and (g) the unit cell of AlB_2 -type BNSLs. (h) Extinction spectra of as-synthesized (blue curve) and DDT-stabilized (red curve) 5.4 nm Ag NCs dispersed in hexanes. (i) Representative normalized extinction spectra taken from a single domain of different superlattices containing DDT-stabilized 5.4 nm Ag NCs. Spectra have been offset vertically for clarity. The optical sampling area is $5.3 \mu\text{m} \times 5.3 \mu\text{m}$ for single-component hcp superlattices and is $3.1 \mu\text{m} \times 3.1 \mu\text{m}$ for BNSLs. All scale bars represent 50 nm.

average nearest-neighbor distance of about 2.1 nm between Ag NCs (Figure 5b and Supporting Information Figure S26) while in the hcp superlattices (Figure 5c and Supporting Information Figure S22), the smallest separation is estimated to be about 1.5 nm based upon the thickness of the NC ligand shell. Importantly, the observed red shifts in the plasmonic resonance of Ag NC-based BNSLs and hcp superlattices are much larger than what's possible with changing the dielectric constants of solvents or varying the size of spherical Ag NCs within the quasi-static regime.²³

In summary, we have studied the collective plasmonic response of self-assembled BNSLs using correlated optical microspectrophotometry and electron microscopy over individual phase-pure BNSL domains. Co-assembly of different types of NC building blocks into multicomponent NC superlattices allows for unprecedented control over the nanoscale arrangement and the strength of near-field couplings of plasmonic NCs, which leads to broadband spectral tunability

of the collective plasmonic resonance. Considering the numerous combinations of NCs and the structural diversity of BNSL phases, self-assembled BNSLs represent a versatile platform for the rational design of macroscopic 3D plasmonic metamaterials exhibiting emerging optical characteristics such as optical chirality, optical magnetism, Fano resonance, and negative index of refraction at optical frequencies.

■ ASSOCIATED CONTENT

Supporting Information

Methods section, additional TEM images and small-angle electron diffraction patterns of single-component Au and Ag NC superlattices and different BNSLs, additional optical micrographs, and extinction spectra collected from multiple individual domains for each superlattice structure. This material is available free of charge via the Internet at <http://pubs.acs.org>.

■ AUTHOR INFORMATION

Corresponding Author

*E-mail: cbmurray@sas.upenn.edu.

Notes

The authors declare no competing financial interest.

■ ACKNOWLEDGMENTS

X.Y. and C.B.M. acknowledge primary support from the Office of Naval Research (ONR) Multidisciplinary University Research Initiative (MURI) on Optical Metamaterials through award N00014-10-1-0942. J.C. acknowledges support from DOE Office of ARPA-E under award DE-AR0000123 for the development of magnetic nanocrystal synthesis and purification and the subsequent support of MRSEC program of the National Science Foundation under award #DMR 11-20901 for synthesis of semiconductor nanocrystals, exploration of superlattice assembly methods, and structural characterization. We are grateful to Northrop Grumman for the resources to build the microspectrophotometry system. B.T.D.'s work on the synthesis of semiconductor nanocrystals was supported in part by U.S. Department of Energy Office of Basic Energy Sciences, Division of Materials Science and Engineering, under award No. DE-SC0002158 and also benefited from the support of IBM Ph.D. Fellowship Award. C.B.M. is also grateful to the Richard Perry University Professorship for support of his supervisor role.

■ REFERENCES

- (1) Halas, N. J.; Lal, S.; Chang, W.-S.; Link, S.; Nordlander, P. *Chem. Rev.* **2011**, *111*, 3913–3961.
- (2) Quinten, M.; Kreibig, U. *Surf. Sci.* **1986**, *172*, 557–577.
- (3) Elghanian, R.; Storhoff, J. J.; Mucic, R. C.; Letsinger, R. L.; Mirkin, C. A. *Science* **1997**, *277*, 1078–1081.
- (4) Kelly, K. L.; Coronado, E.; Zhao, L. L.; Schatz, G. C. *J. Phys. Chem. B* **2003**, *107*, 668–677.
- (5) Prodan, E.; Radloff, C.; Halas, N. J.; Nordlander, P. *Science* **2003**, *302*, 419–422.
- (6) Jain, P. K.; Huang, W. Y.; El-Sayed, M. A. *Nano Lett.* **2007**, *7*, 2080–2088.
- (7) Lal, S.; Grady, N. K.; Kundu, J.; Levin, C. S.; Lassiter, J. B.; Halas, N. J. *Chem. Soc. Rev.* **2008**, *37*, 898–911.
- (8) Alvarez-Puebla, R. A.; Agarwal, A.; Manna, P.; Khanal, B. P.; Aldeanueva-Potel, P.; Carbó-Argibay, E.; Pazos-Pérez, N.; Vigderman, L.; Zubarev, E. R.; Kotov, N. A.; Liz-Marzán, L. M. *Proc. Natl. Acad. Sci. U.S.A.* **2011**, *108*, 8157–8161.
- (9) Kabashin, A. V.; Evans, P.; Pastkovsky, S.; Hendren, W.; Wurtz, G. A.; Atkinson, R.; Pollard, R.; Podolskiy, V. A.; Zayats, A. V. *Nat. Mater.* **2009**, *8*, 867–871.
- (10) Sonnichsen, C.; Reinhard, B. M.; Liphardt, J.; Alivisatos, A. P. *Nat. Biotechnol.* **2005**, *23*, 741–745.
- (11) Liu, N.; Hentschel, M.; Weiss, T.; Alivisatos, A. P.; Giessen, H. *Science* **2011**, *332*, 1407–1410.
- (12) Fan, J. A.; Wu, C. H.; Bao, K.; Bao, J. M.; Bardhan, R.; Halas, N. J.; Manoharan, V. N.; Nordlander, P.; Shvets, G.; Capasso, F. *Science* **2010**, *328*, 1135–1138.
- (13) Luk'yanchuk, B.; Zheludev, N. I.; Maier, S. A.; Halas, N. J.; Nordlander, P.; Giessen, H.; Chong, C. T. *Nat. Mater.* **2010**, *9*, 707–715.
- (14) Sheikholeslami, S. N.; Garcia-Etxarri, A.; Dionne, J. A. *Nano Lett.* **2011**, *11*, 3927–3934.
- (15) Alaeian, H.; Dionne, J. A. *Opt. Express* **2012**, *20*, 15781–15796.
- (16) Yan, B.; Thubagere, A.; Premasiri, W. R.; Ziegler, L. D.; Dal Negro, L.; Reinhard, B. M. *ACS Nano* **2009**, *3*, 1190–1202.
- (17) Lubin, S. M.; Zhou, W.; Hryni, A. J.; Huntington, M. D.; Odom, T. W. *Nano Lett.* **2012**, *12*, 4948–4952.
- (18) Ye, J.; Wen, F. F.; Sobhani, H.; Lassiter, J. B.; Van Dorpe, P.; Nordlander, P.; Halas, N. J. *Nano Lett.* **2012**, *12*, 1660–1667.
- (19) Taleb, A.; Petit, C.; Pileni, M. P. *J. Phys. Chem. B* **1998**, *102*, 2214–2220.
- (20) Sun, Y. G.; Xia, Y. N. *Science* **2002**, *298*, 2176–2179.
- (21) Tao, A.; Sinsermsuksakul, P.; Yang, P. *Nat. Nanotechnol.* **2007**, *2*, 435–440.
- (22) Chen, C. F.; Tzeng, S. D.; Chen, H. Y.; Lin, K. J.; Gwo, S. *J. Am. Chem. Soc.* **2008**, *130*, 824–826.
- (23) Peng, S.; McMahon, J. M.; Schatz, G. C.; Gray, S. K.; Sun, Y. G. *Proc. Natl. Acad. Sci. U.S.A.* **2010**, *107*, 14530–14534.
- (24) Rycenga, M.; Cobley, C. M.; Zeng, J.; Li, W. Y.; Moran, C. H.; Zhang, Q.; Qin, D.; Xia, Y. N. *Chem. Rev.* **2011**, *111*, 3669–3712.
- (25) Gwo, S.; Lin, M. H.; He, C. L.; Chen, H. Y.; Teranishi, T. *Langmuir* **2012**, *28*, 8902–8908.
- (26) Barrow, S. J.; Wei, X.; Baldauf, J. S.; Funston, A. M.; Mulvaney, P. *Nat. Commun.* **2012**, *3*, 1275.
- (27) Xu, L. G.; Kuang, H.; Xu, C. L.; Ma, W.; Wang, L. B.; Kotov, N. A. *J. Am. Chem. Soc.* **2012**, *134*, 1699–1709.
- (28) Goubet, N.; Portales, H.; Yan, C.; Arfaoui, I.; Albouy, P.-A.; Mermet, A.; Pileni, M.-P. *J. Am. Chem. Soc.* **2012**, *134*, 3714–3719.
- (29) Ye, X.; Jin, L. H.; Caglayan, H.; Chen, J.; Xing, G. Z.; Zheng, C.; Vicki, D. N.; Kang, Y. J.; Engheta, N.; Kagan, C. R.; Murray, C. B. *ACS Nano* **2012**, *6*, 2804–2817.
- (30) Ye, X.; Zheng, C.; Chen, J.; Gao, Y.; Murray, C. B. *Nano Lett.* **2013**, *13*, 765–771.
- (31) Shemer, G.; Krichevski, O.; Markovich, G.; Molotsky, T.; Lubitz, I.; Kotlyar, A. B. *J. Am. Chem. Soc.* **2006**, *128*, 11006–11007.
- (32) Jones, M. R.; Macfarlane, R. J.; Lee, B.; Zhang, J. A.; Young, K. L.; Senesi, A. J.; Mirkin, C. A. *Nat. Mater.* **2010**, *9*, 913–917.
- (33) Shevchenko, E. V.; Talapin, D. V.; Kotov, N. A.; O'Brien, S.; Murray, C. B. *Nature* **2006**, *439*, 55–59.
- (34) Urban, J. J.; Talapin, D. V.; Shevchenko, E. V.; Kagan, C. R.; Murray, C. B. *Nat. Mater.* **2007**, *6*, 115–121.
- (35) Shevchenko, E. V.; Ringler, M.; Schwemer, A.; Talapin, D. V.; Klar, T. A.; Rogach, A. L.; Feldmann, J.; Alivisatos, A. P. *J. Am. Chem. Soc.* **2008**, *130*, 3274–3275.
- (36) Smith, D. K.; Goodfellow, B.; Smilgies, D. M.; Korgel, B. A. *J. Am. Chem. Soc.* **2009**, *131*, 3281–3290.
- (37) Dong, A.; Chen, J.; Vora, P. M.; Kikkawa, J. M.; Murray, C. B. *Nature* **2010**, *466*, 474–477.
- (38) Bodnarchuk, M. I.; Kovalenko, M. V.; Heiss, W.; Talapin, D. V. *J. Am. Chem. Soc.* **2010**, *132*, 11967–11977.
- (39) Evers, W. H.; De Nijs, B.; Filion, L.; Castillo, S.; Dijkstra, M.; Vanmaekelbergh, D. *Nano Lett.* **2010**, *10*, 4235–4241.
- (40) Chen, J.; Dong, A. G.; Cai, J.; Ye, X.; Kang, Y. J.; Kikkawa, J. M.; Murray, C. B. *Nano Lett.* **2010**, *10*, 5103–5108.
- (41) Ye, X.; Chen, J.; Murray, C. B. *J. Am. Chem. Soc.* **2011**, *133*, 2613–2620.

- (42) Nagaoka, Y.; Chen, O.; Wang, Z.; Cao, Y. *C. J. Am. Chem. Soc.* **2012**, *134*, 2868–2871.
- (43) Ye, X.; Collins, J. E.; Kang, Y. J.; Chen, J.; Chen, D. T. N.; Yodh, A. G.; Murray, C. B. *Proc. Natl. Acad. Sci. U.S.A.* **2010**, *107*, 22430–22435.
- (44) Chen, J.; Ye, X.; Murray, C. B. *ACS Nano* **2010**, *4*, 2374–2381.
- (45) Su, K. H.; Wei, Q. H.; Zhang, X.; Mock, J. J.; Smith, D. R.; Schultz, S. *Nano Lett.* **2003**, *3*, 1087–1090.
- (46) Chen, Z. Y.; Moore, J.; Radtke, G.; Sirringhaus, H.; O'Brien, S. J. *Am. Chem. Soc.* **2007**, *129*, 15702–15709.
- (47) Maier, S. A.; Kik, P. G.; Atwater, H. A.; Meltzer, S.; Harel, E.; Koel, B. E.; Requicha, A. A. G. *Nat. Mater.* **2003**, *2*, 229–232.
- (48) Linnert, T.; Mulvaney, P.; Henglein, A. *J. Phys. Chem.* **1993**, *97*, 679–682.
- (49) Zijlstra, P.; Paulo, P. M. R.; Yu, K.; Xu, Q. H.; Orrit, M. *Angew. Chem., Int. Ed.* **2012**, *51*, 8352–8355.

Tunable Plasmonic Coupling in Self-Assembled Binary Nanocrystal Superlattices Studied by Correlated Optical Microspectrophotometry and Electron Microscopy

Xingchen Ye¹, Jun Chen¹, Benjamin T. Diroll¹, Christopher B. Murray^{1, 2}*

¹Department of Chemistry and ²Department of Materials Science and Engineering, University of Pennsylvania, Pennsylvania 19104, United States.

Methods

NC Synthesis. Monodisperse (< 5% standard deviation in size) PbS,¹ PbTe,² Fe₃O₄,³ 5.5 nm dodecanethiol-stabilized Au⁴ and 9.7 nm oleylamine-stabilized Au NCs⁵ were synthesized according to previously reported methods. All NCs were finally dispersed in hexane as stable colloidal solutions for superlattice formation. Monodisperse Ag NCs were synthesized using a CEM Discover microwave reactor running in open-vessel mode. Typically, 1 mmol tetradecylphosphonic acid (PCI synthesis), 2 mmol silver acetate (Aldrich) and 20 ml trioctylamine (Aldrich) were loaded into a 50 mL round-bottomed flask. Under nitrogen atmosphere and vigorous stirring, the reaction mixture was heated by microwave irradiation (150 W) to 150 °C in 4 minutes followed by being kept at 150 °C for another 5 minutes. The reaction flask was air-cooled to room temperature and the NC products were isolated by ethanol precipitation and centrifugation. As-synthesized Ag NCs were surface-modified with 1-dodecanethiol using a similar procedure developed for oleylamine-capped Au NCs.⁴ The dodecanethiol-passivated Ag NCs were finally dispersed in hexane.

Self-Assembly of Plasmonic BNSLs. BNSLs were formed by co-crystallization of two types of NCs on the surface of ethylene glycol (EG) at room temperature. In a typical process, a hexane solution (~ 15 μL) containing two NC components was spread onto the surface of EG in a Teflon well (1.5 × 1.5 × 1.5 cm³). The well was then covered with a glass slide to slow down the evaporation of hexane. After 15 min, the BNSL film was transferred onto carbon-coated Cu TEM grids (300-mesh) that was further dried under vacuum to remove extra EG. Single-component Au and Ag NC superlattices were formed in a similar manner. Using atomic force microscopy, it is found that the thickness of individual BNSL domains typically ranges from 20

nm to 80 nm (depending on the size of the two spherical NC components as well as the crystal structure of BNSLs), which corresponds to 1-4 unit cells along the z-direction.

Structural and Optical Characterization. Transmission electron microscopy (TEM) images and small-angle electron diffraction patterns were acquired on a JEM-1400 microscope operating at 120kV. Optical extinction spectra of NC solutions were taken in transmission mode on a Cary 5000 UV/Vis/NIR spectrophotometer. Extinction spectra of individual nanocrystal superlattice domains and optical images were obtained using a 308 PV microscope spectrophotometer system (Craic Technologies) integrated on an Olympus BX51 upright optical microscope. TEM grids with NC superlattices were placed onto a glass slide. Samples were illuminated from the bottom side by unpolarized white light from a 100 W tungsten-halogen lamp, and the transmitted light was collected using either a 50x (MPlanFL, NA 0.80) or a 100x (LMPlanFL, NA 0.80) objective lens (depending on the size of superlattice domains), focused onto the entrance aperture of the spectrophotometer and measured by a CCD detector. Since the aperture is mirrored, the majority of light is directed towards a digital imaging system, which allows for visualization of the spectrophotometer aperture (an example is shown as the black square in Figure 1a) overlaid on the sample and makes it convenient to move to regions of interest and collect spectra. Reference spectra were recorded from a carbon-coated TEM grid without deposited NCs. The optical sampling area depends on the power of the objective lens: 3.1 μ m x 3.1 μ m for a 100x objective lens and 5.3 μ m x 5.3 μ m for a 50x objective lens. Each spectrum represents an average of 25 scans. Optical extinction measurements are performed over at least 10 different domains for each BNSL structure to ensure spectral consistency.

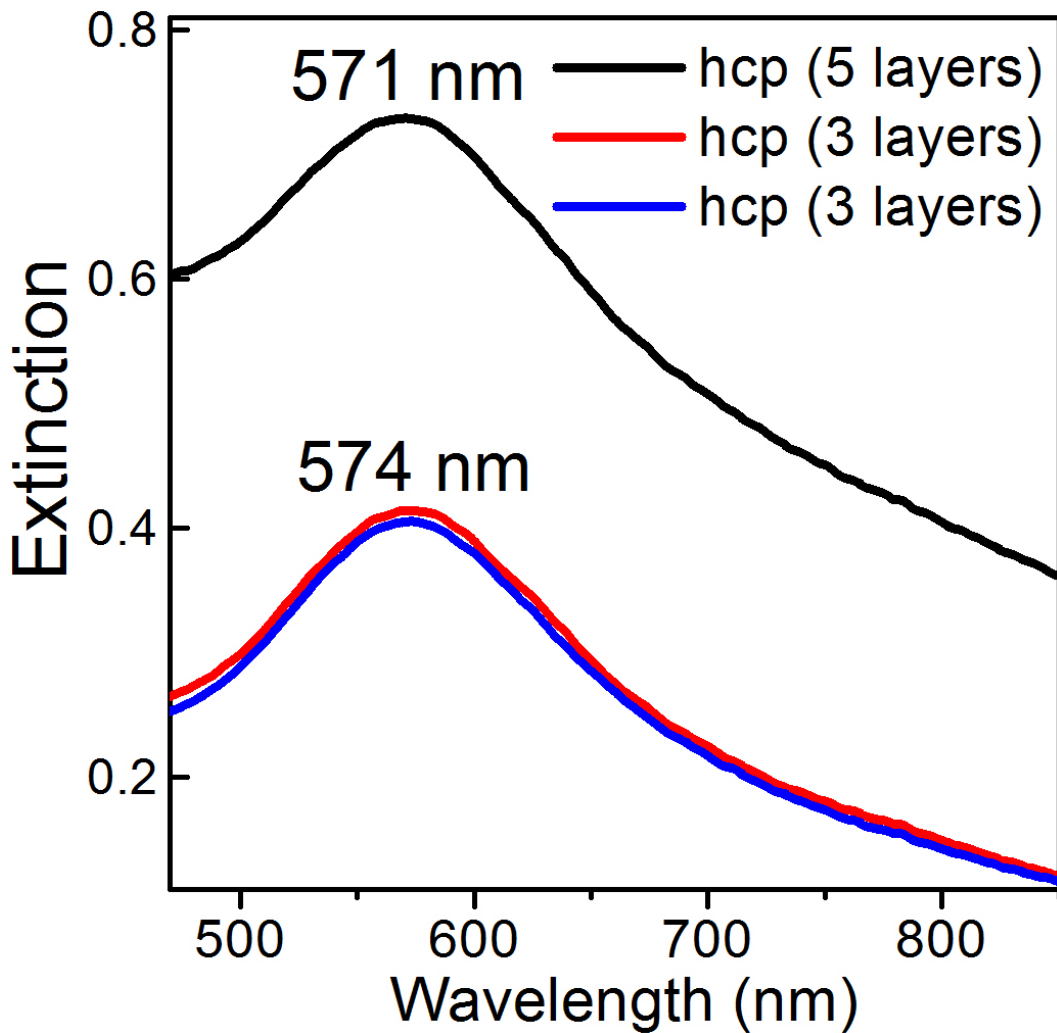


Figure S1. Extinction spectra of hexagonal close-packed (hcp) superlattices of 5.5 nm dodecanethiol-stabilized Au NCs. Representative spectra collected from different thinner (red and blue curves, three layers thick) and thicker superlattice domains (black curve, five layers thick) are presented. A 50x objective lens is used and the optical sampling area is 5.3 μm x 5.3 μm .

#

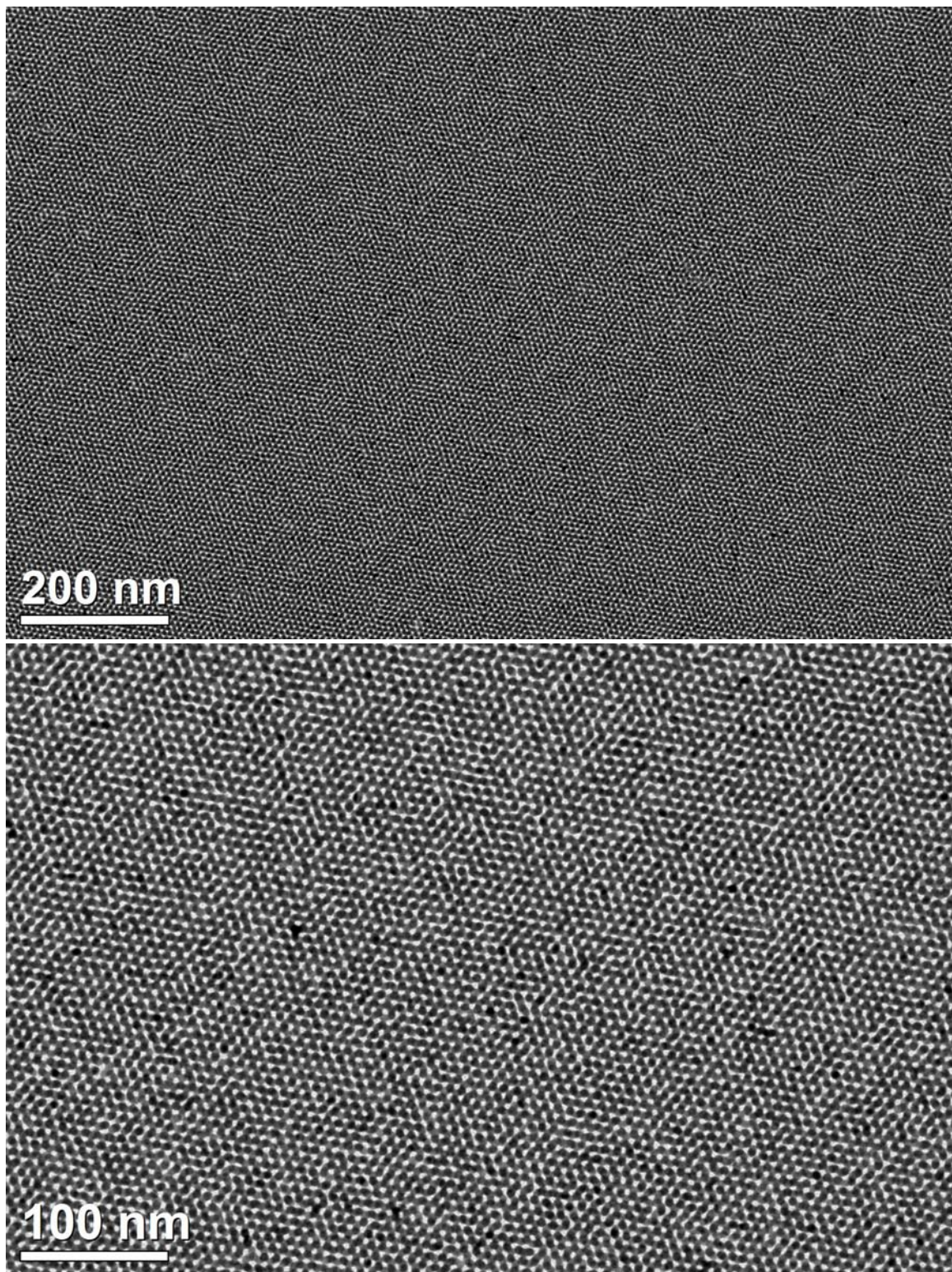


Figure S2. TEM images of hcp superlattices (three layers thick) of 5.5 nm dodecanethiol-stabilized Au NCs.

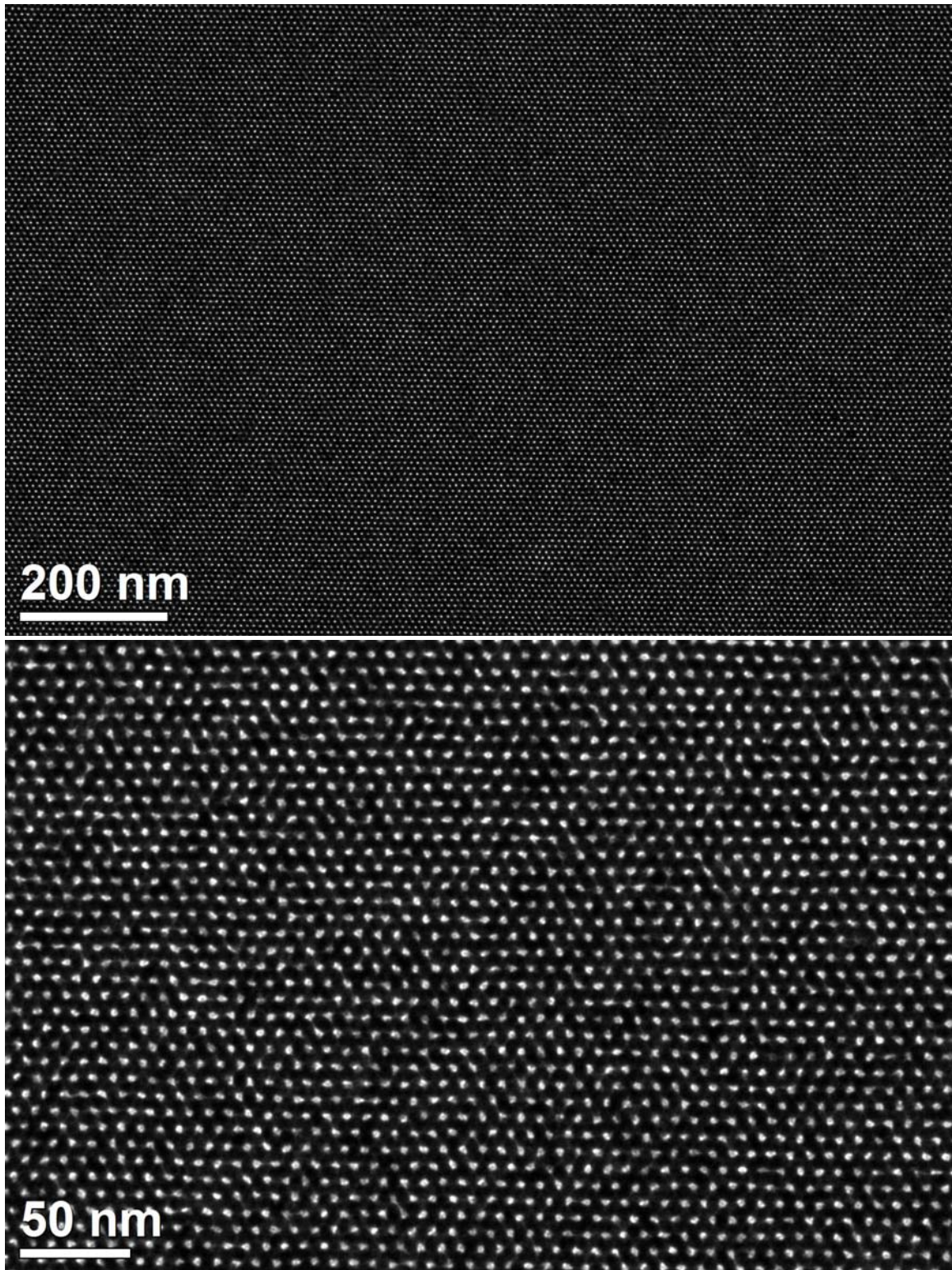


Figure S3. TEM images of hcp superlattices (five layers thick) of 5.5 nm dodecanethiol-stabilized Au NCs.

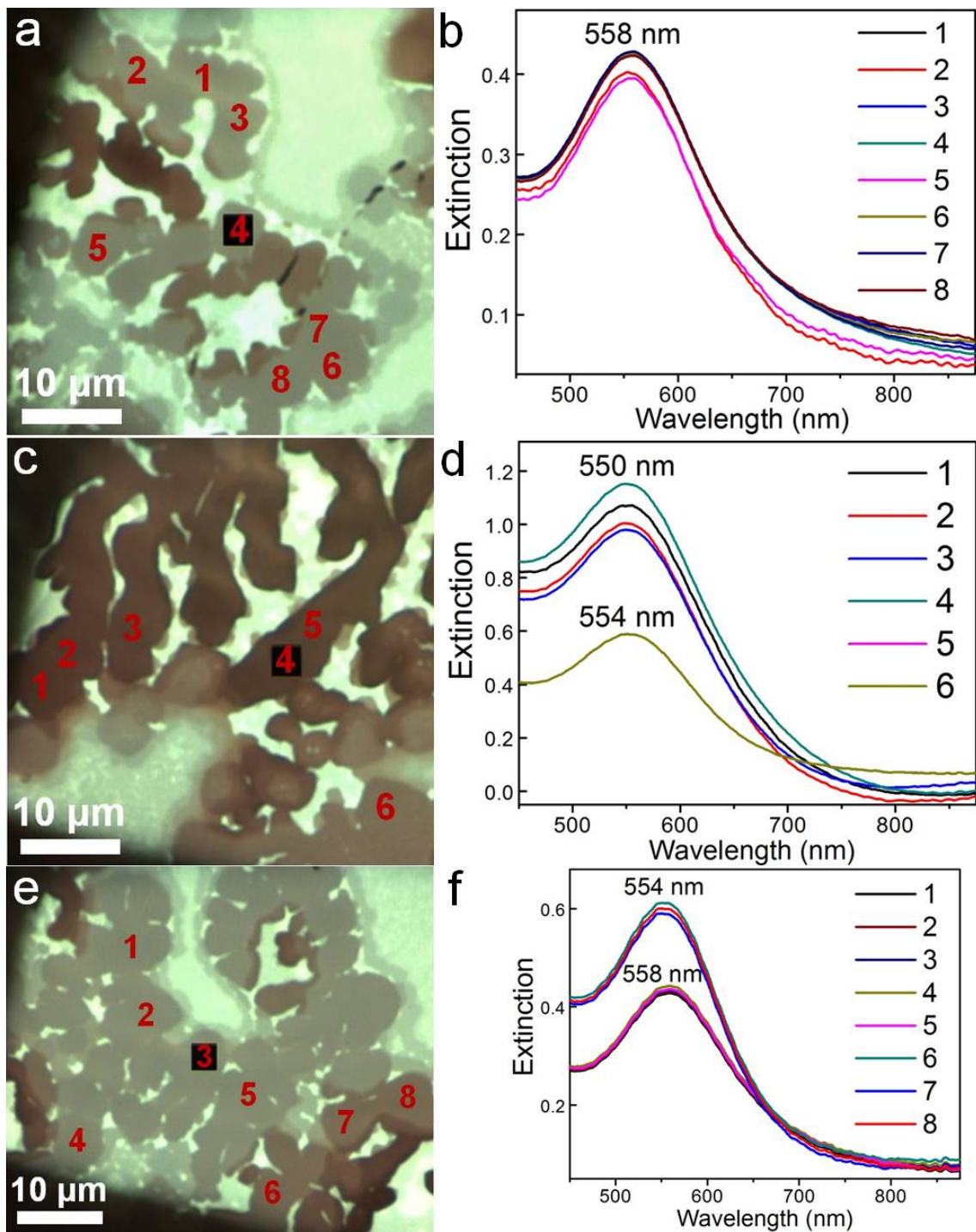


Figure S4. (a, c, e) Optical micrographs of NaZn₁₃-type BNSLs self-assembled from 5.5 nm dodecanethiol-stabilized Au NCs and 9.3 nm PbS NCs. (b, d, f) Extinction spectra collected from different single-crystalline BNSL domains as labelled in the corresponding optical micrographs. A 100x objective lens is used and the optical sampling area is 3.1 μm x 3.1 μm.

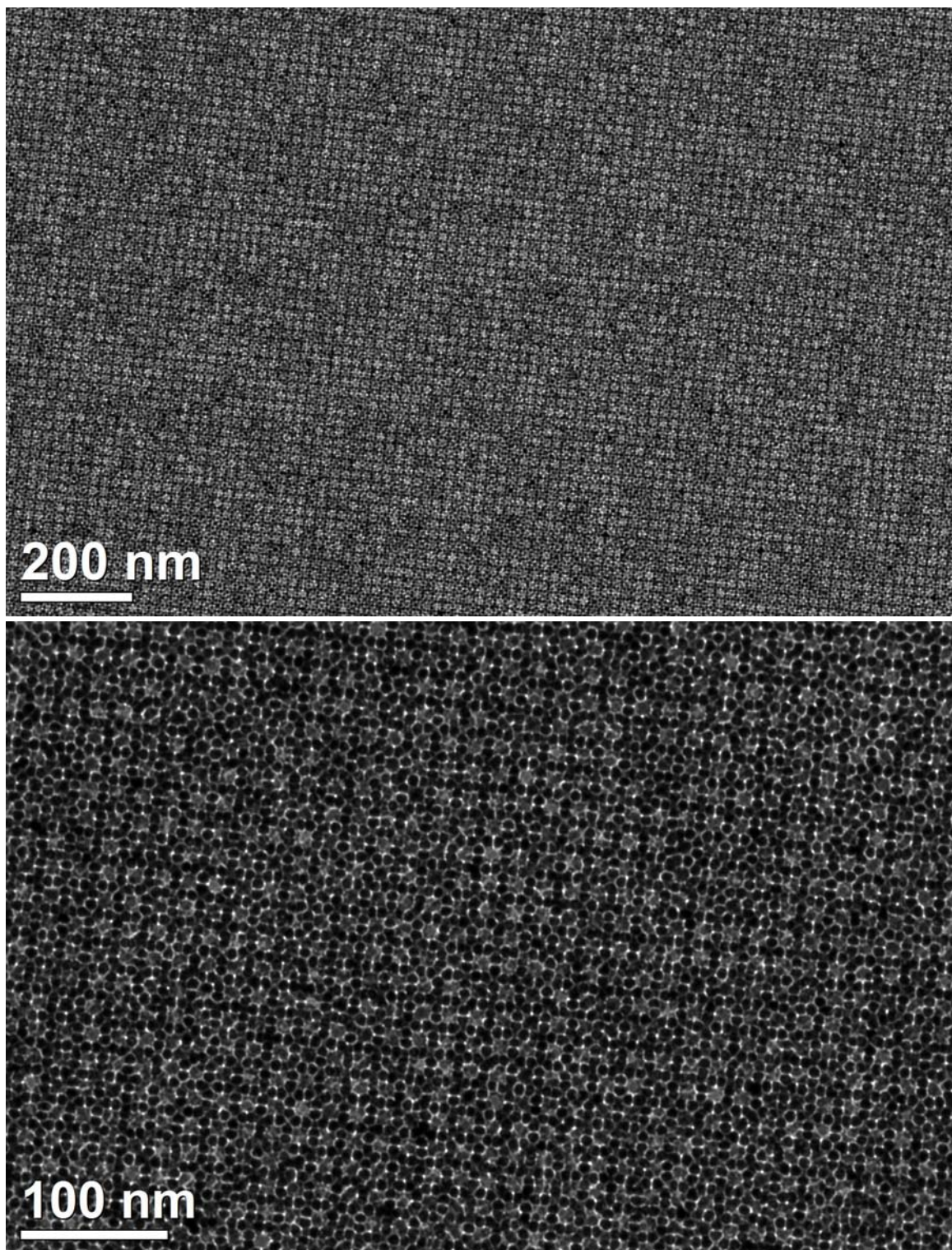


Figure S5. TEM images of NaZn₁₃-type BNSLs self-assembled from 5.5 nm dodecanethiol-stabilized Au NCs and 9.3 nm PbS NCs.

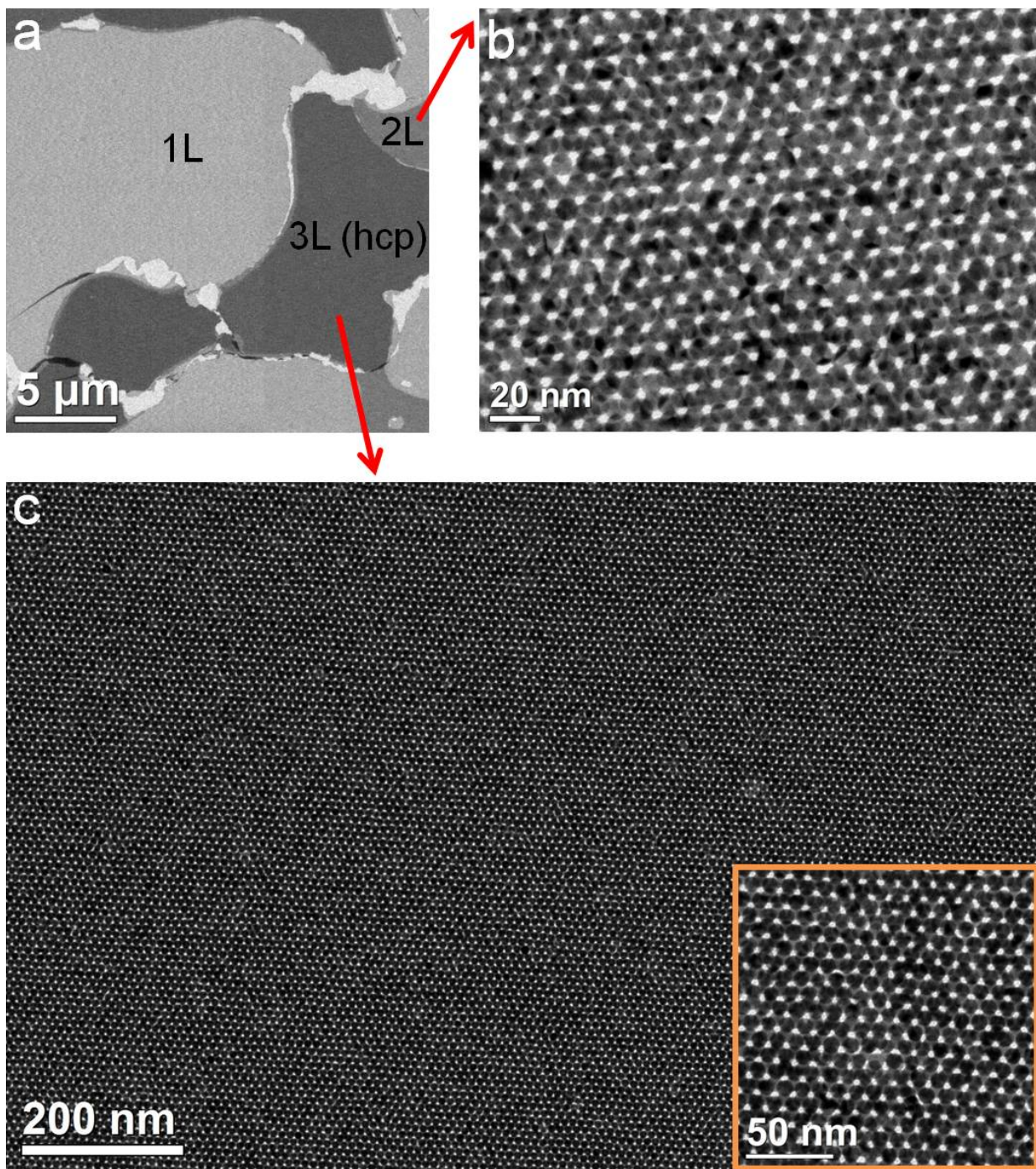


Figure S6. (a) Low-magnification TEM image of 9.7 nm oleylamine-stabilized Au NC superlattices with different thicknesses. 1L: monolayer, 2L: bilayer, 3L: hcp superlattices that are three layers thick. (b, c) TEM images of (b) bilayered and (c) hcp superlattices that are three layers thick. Inset of (c): High-magnification TEM image of the hcp superlattices.

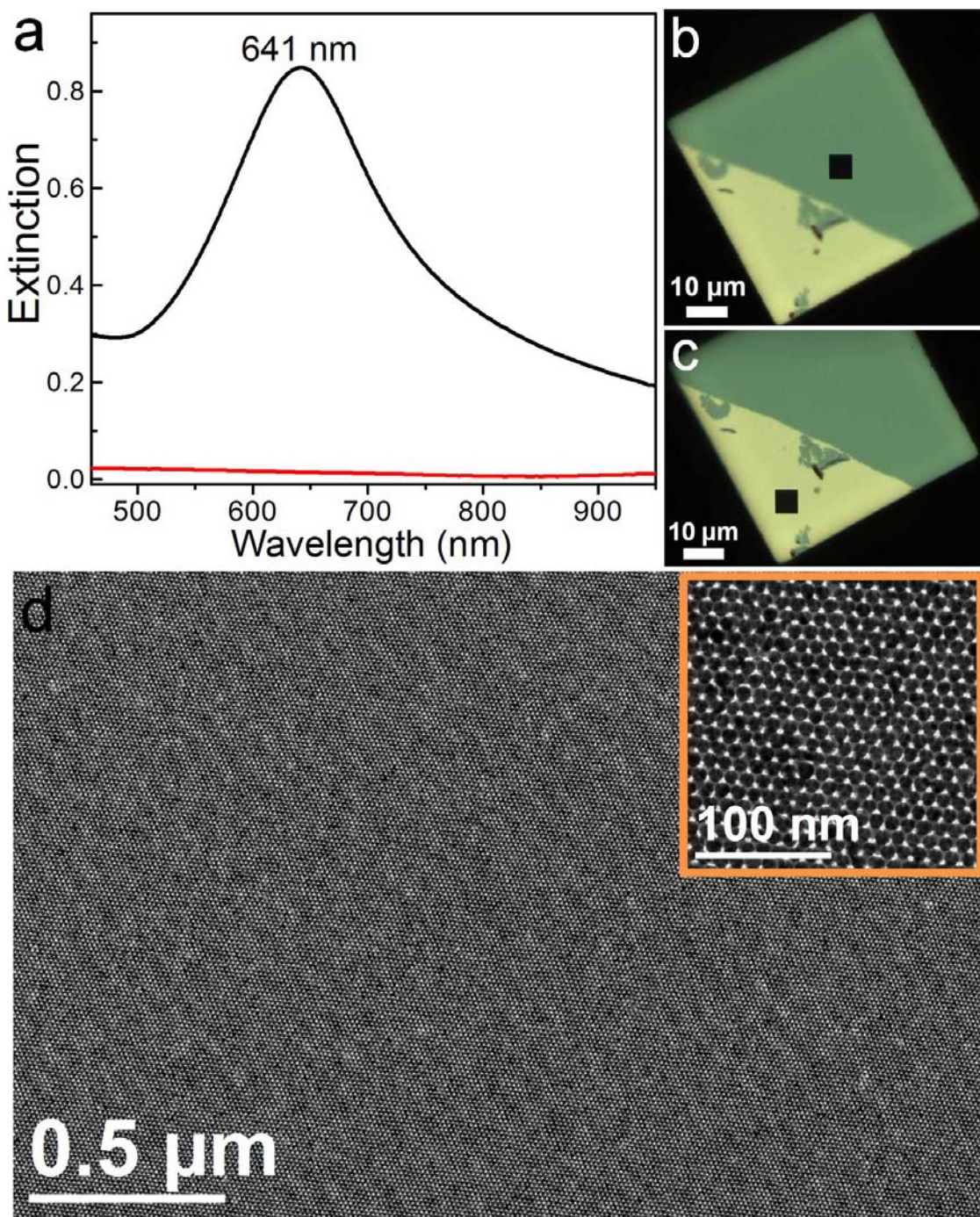


Figure S7. (a) Extinction spectra of hcp superlattices (three layers thick) of 9.7 nm oleylamine-stabilized Au NCs (black curve) collected from part (indicated by the black square in (b)) of a continuous Au NC superlattice film. The extinction spectra recorded from the carbon film region that is free of NCs (indicated by the black square in (c)) is also shown in (a) (red curve). (d) TEM image and a magnified view (inset) of hcp superlattices (three layers thick) of 9.7 nm oleylamine-stabilized Au NCs taken from the same area as shown in (b). A 50x objective lens is used and the optical sampling area is 5.3 $\mu\text{m} \times 5.3 \mu\text{m}$.

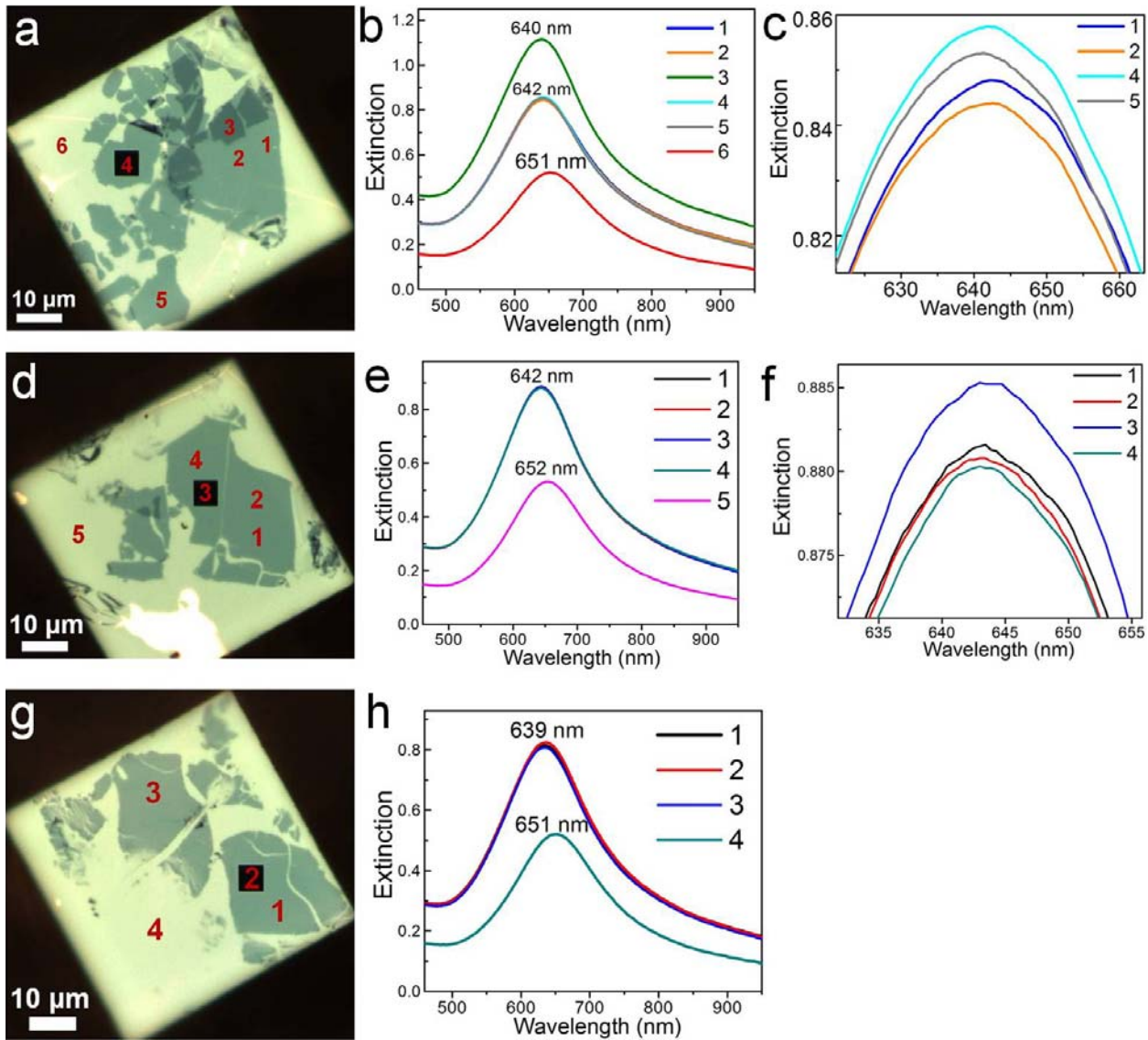


Figure S8. (a, d, g) Optical micrographs of self-assembled superlattices of 9.7 nm oleylamine-stabilized Au NCs. (b, e, h) Extinction spectra collected from different superlattice domains as labelled in the corresponding optical micrographs. (c) and (f) are magnified views of LSPR peaks of the spectra shown in (b) and (e), respectively. The light regions in the optical micrographs such as region 6 in (a), region 5 in (d) and region 4 in (g) are confirmed to be bilayered superlattices by TEM. A 50x objective lens is used and the optical sampling area is 5.3 μm x 5.3 μm.

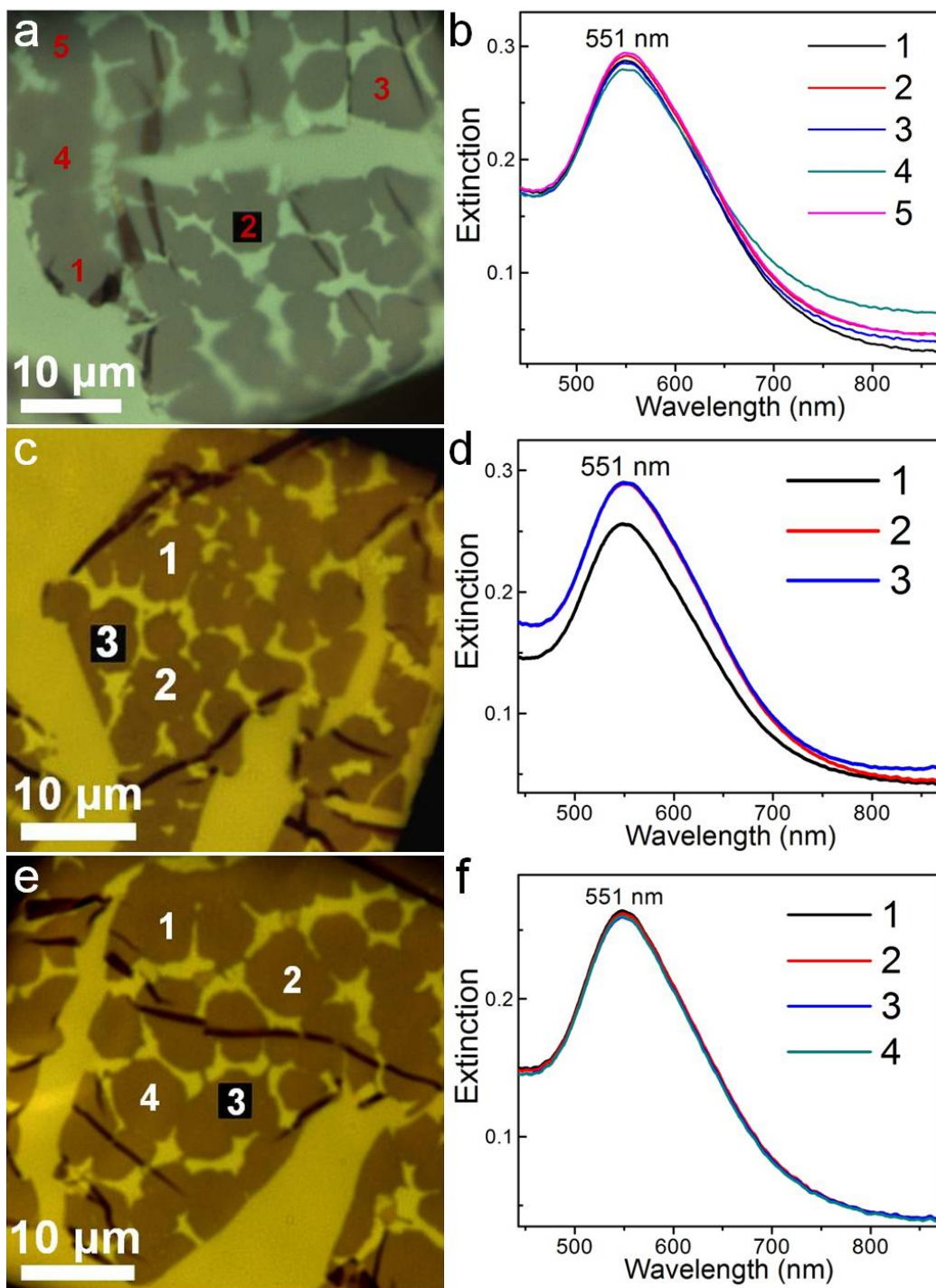


Figure S9. (a, c, e) Optical micrographs of MgZn₂-type BNSLs self-assembled from 9.7 nm oleylamine-stabilized Au NCs and 5.8 nm PbTe NCs. (b, d, f) Extinction spectra collected from different single-crystalline BNSL domains as labelled in the corresponding optical micrographs. A 100x objective lens is used and the optical sampling area is 3.1 μm x 3.1 μm.

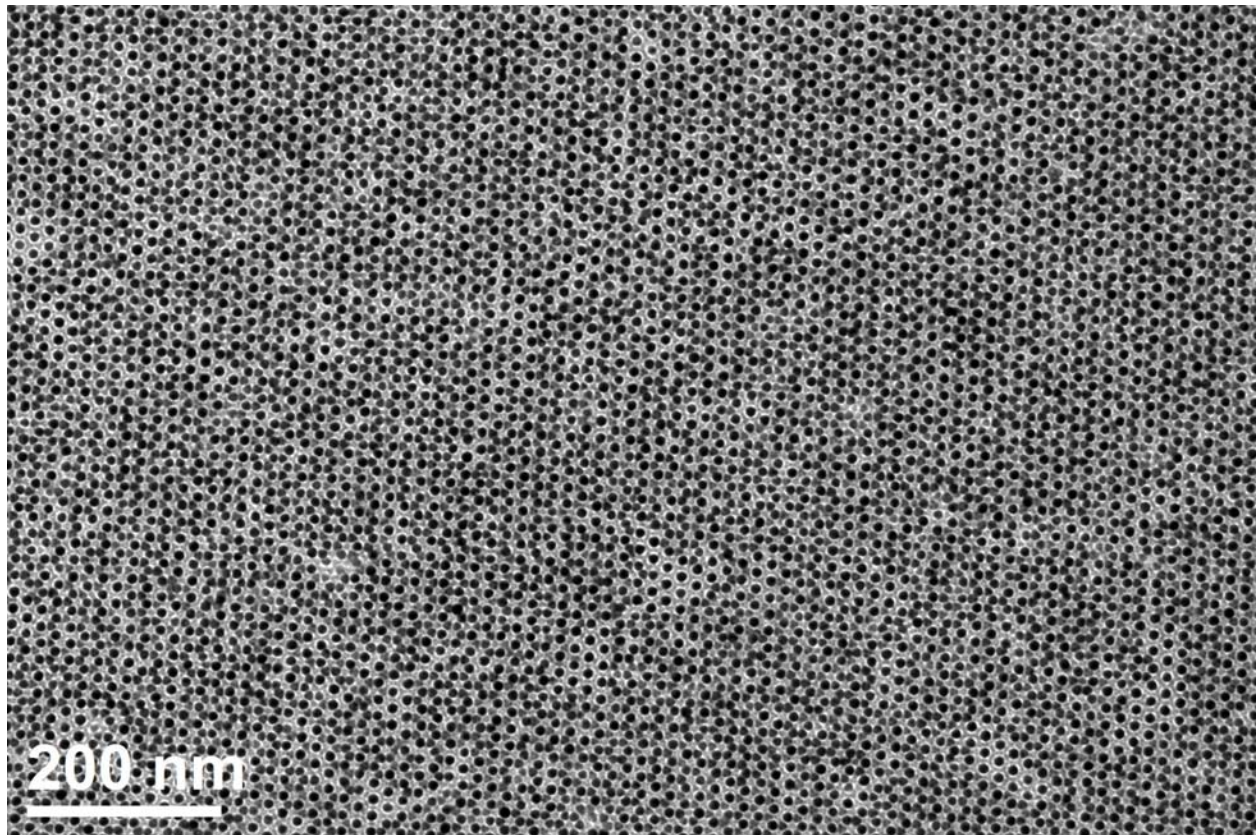


Figure S10. Representative TEM image of MgZn₂-type BNSLs self-assembled from 9.7 nm oleylamine-stabilized Au NCs and 5.8 nm PbTe NCs.

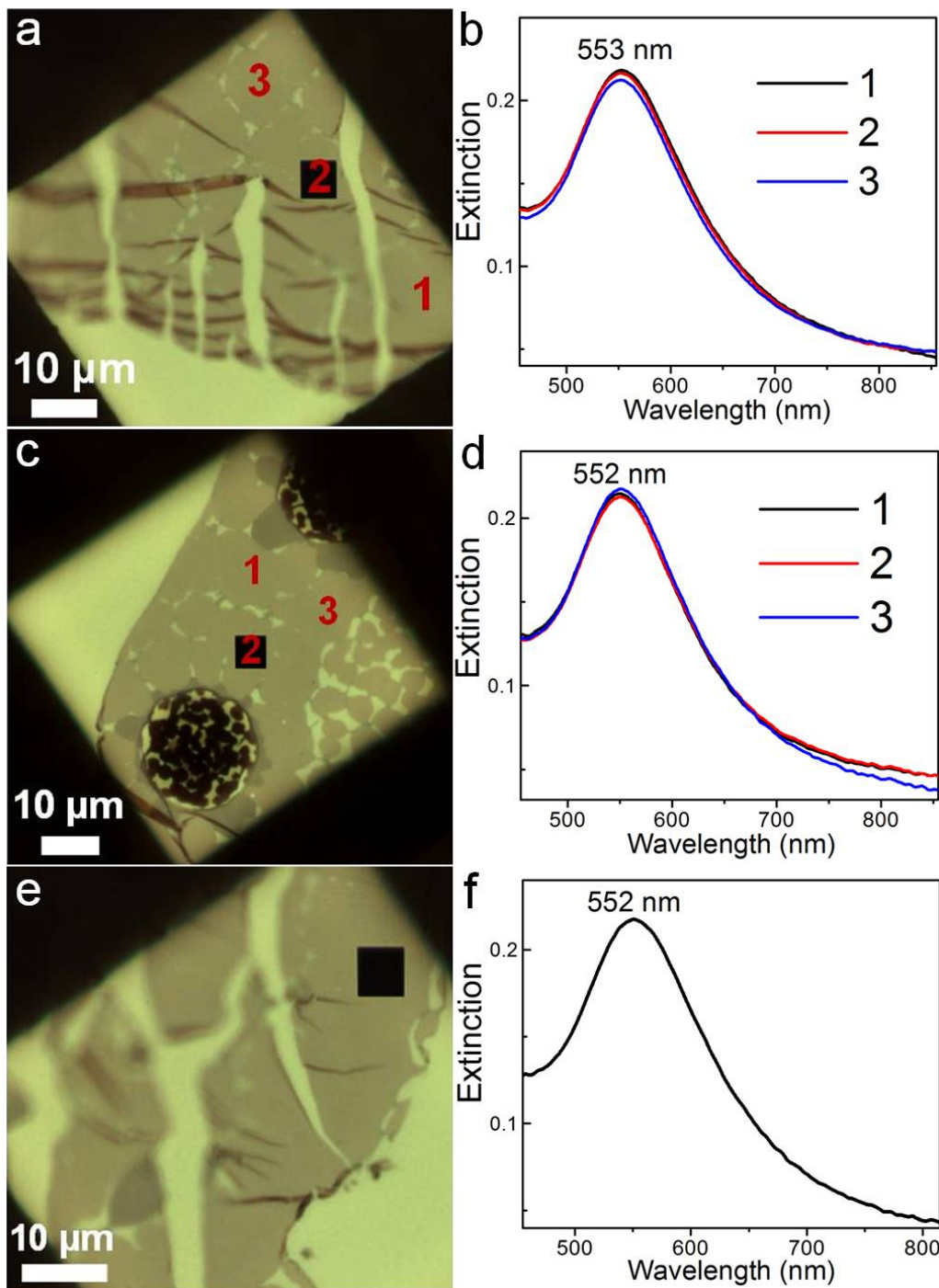


Figure S11. (a, c, e) Optical micrographs of CaCu₅-type BNSLs self-assembled from 9.7 nm oleylamine-stabilized Au NCs and 5.8 nm PbTe NCs. (b, d, f) Extinction spectra collected from different single-crystalline BNSL domains as labelled in the corresponding optical micrographs. A 50x objective lens is used and the optical sampling area is 5.3 $\mu\text{m} \times 5.3 \mu\text{m}$.

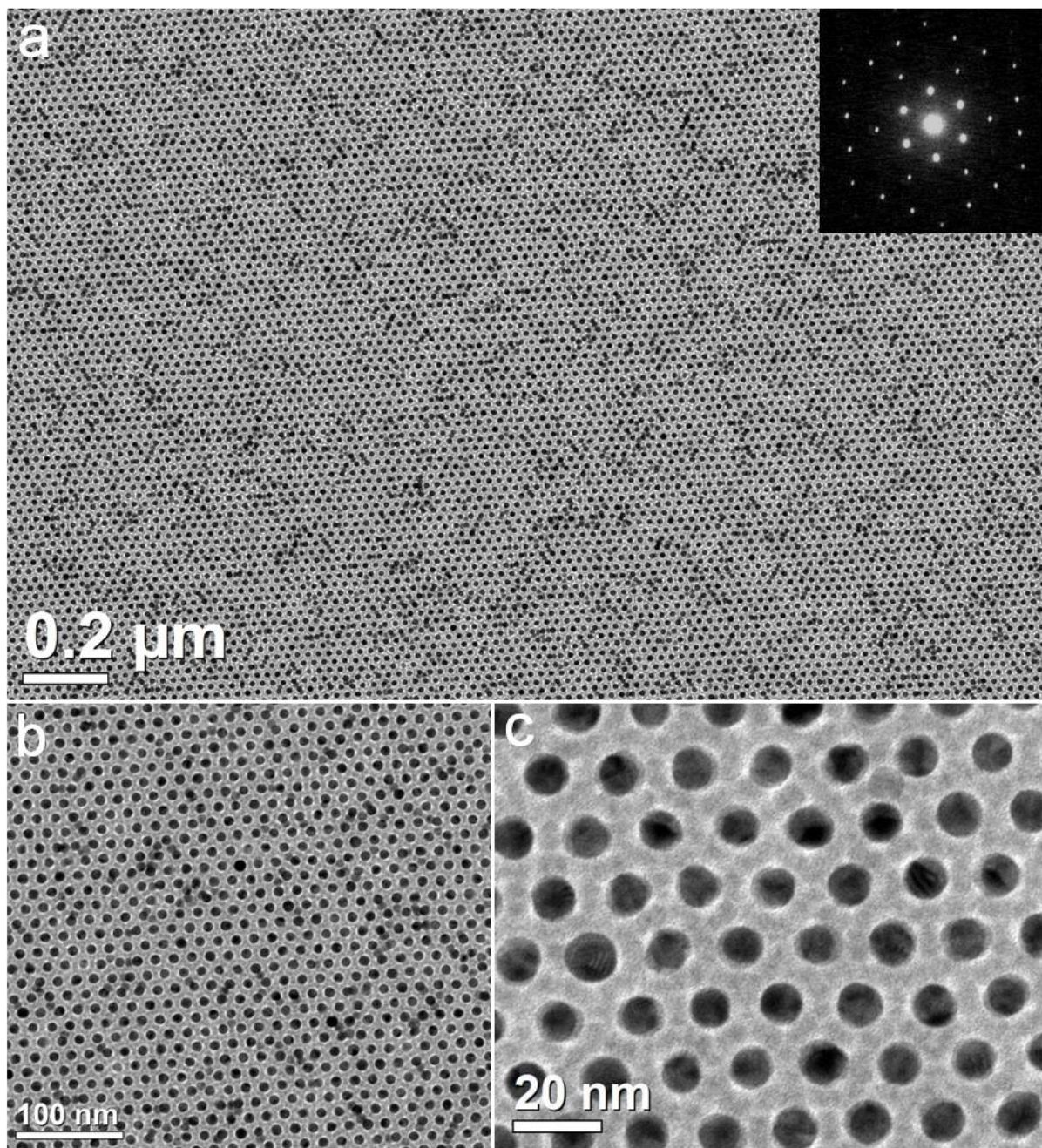


Figure S12. (a) Low-magnification and (b, c) high-magnification TEM images of CaCu_5 -type BNSLs self-assembled from 9.7 nm oleylamine-stabilized Au NCs and 5.8 nm PbTe NCs. Inset of (a) shows the corresponding small-angle electron diffraction pattern.

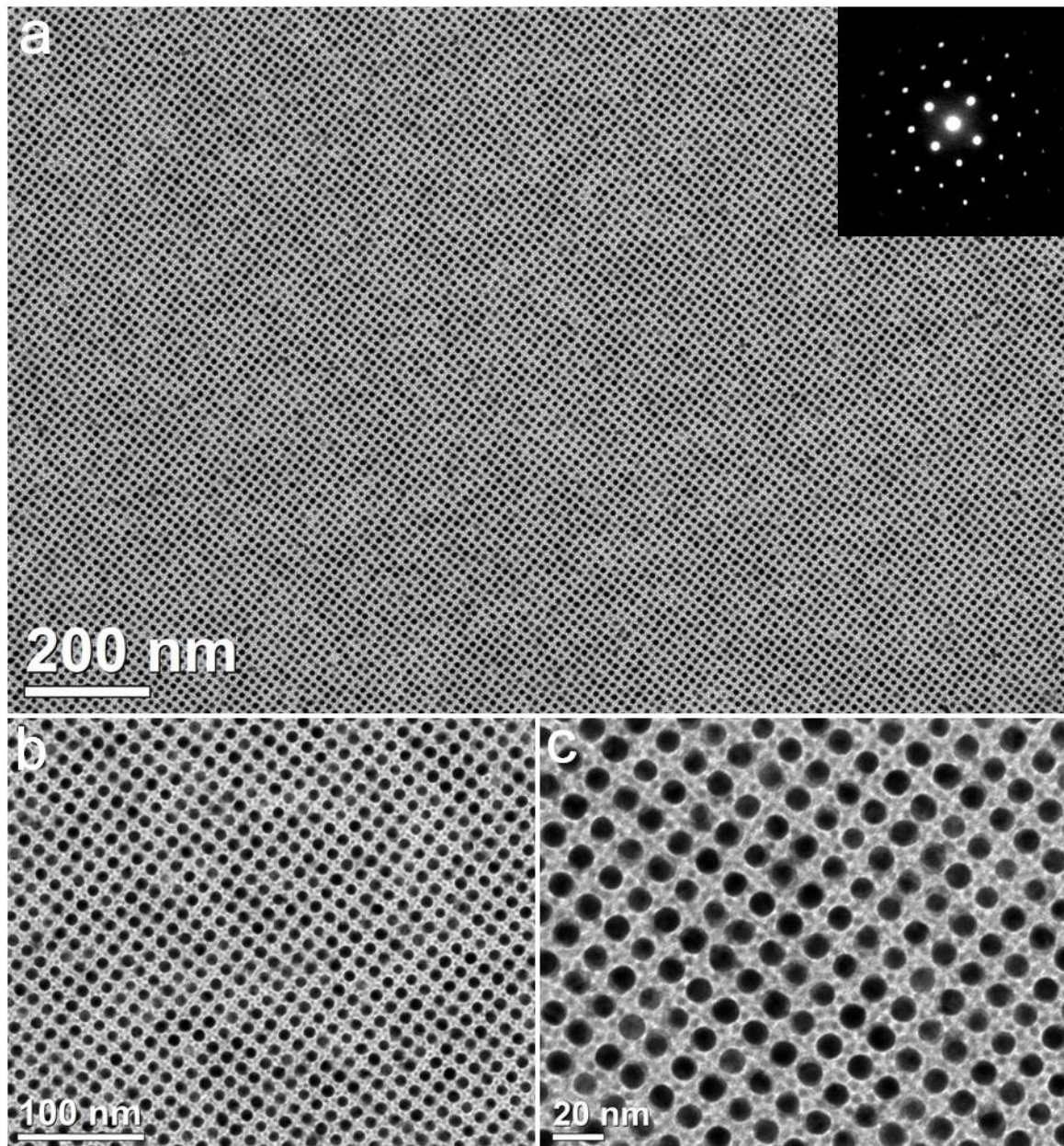


Figure S13. (a) Low-magnification and (b, c) high-magnification TEM images of NaZn₁₃-type BNSLs self-assembled from 9.7 nm oleylamine-stabilized Au NCs and 3.8 nm PbS NCs. Inset of (a) shows the corresponding small-angle electron diffraction pattern.

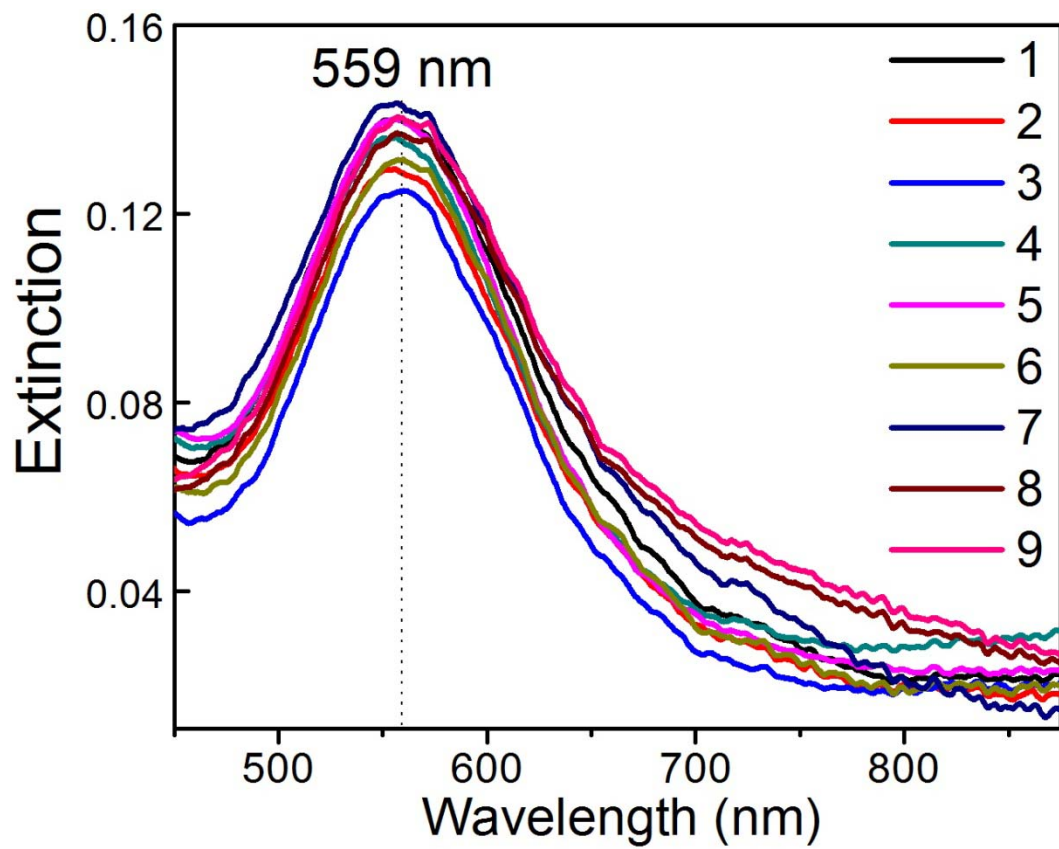


Figure S14. Extinction spectra collected from nine different single-crystalline NaZn₁₃-type BNSL domains self-assembled from 9.7 nm oleylamine-stabilized Au NCs and 3.8 nm PbS NCs. A 100x objective lens is used and the optical sampling area is 3.1 μm x 3.1 μm .

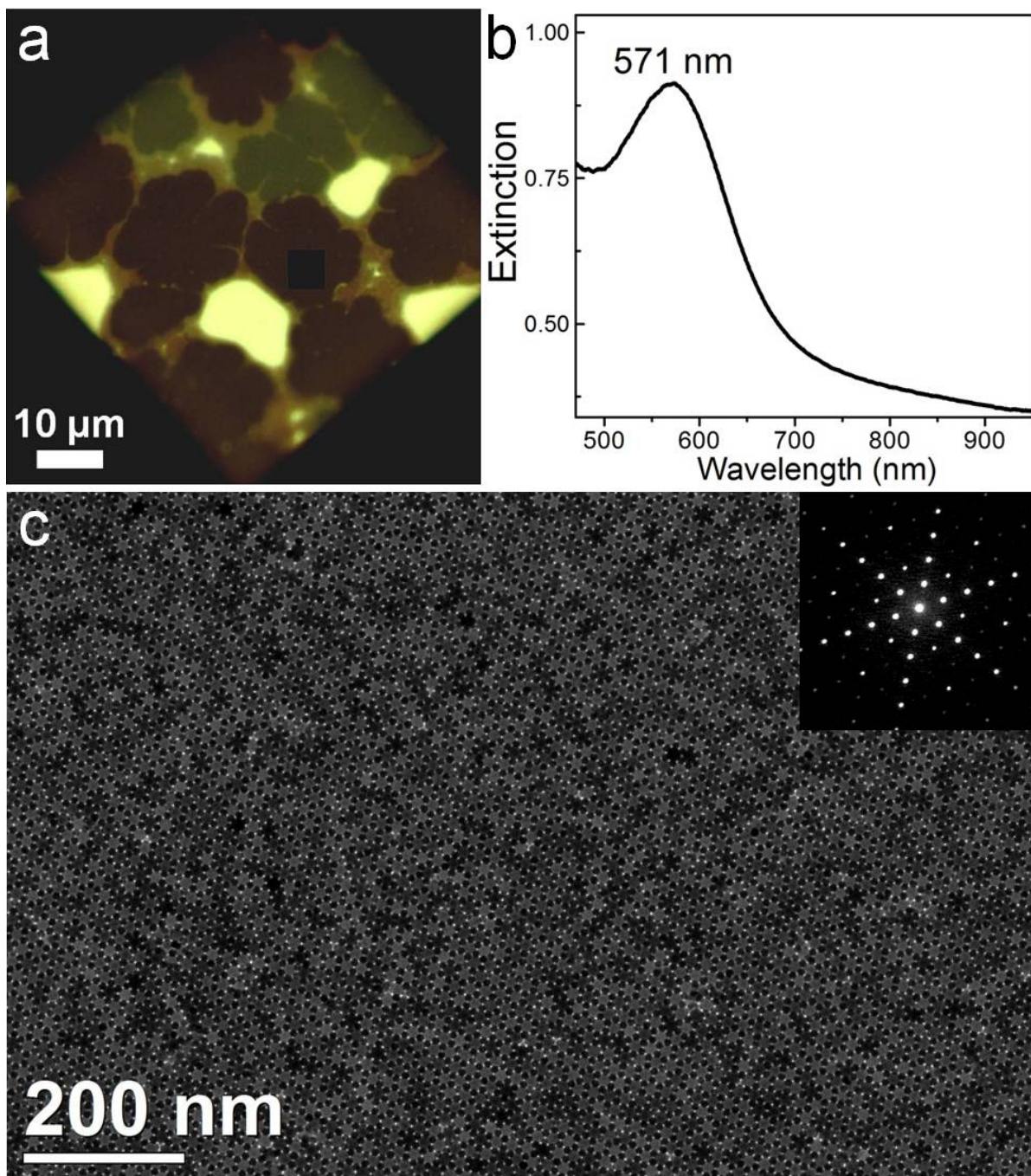


Figure S15. (a) Optical micrographs of AlB₂-type BNSLs self-assembled from 9.7 nm oleylamine-stabilized Au NCs and 17.1 nm Fe₃O₄ NCs. (b) Extinction spectra collected from a single AlB₂-type BNSL domain as indicated by the black square in (a). (c) TEM image and small-angle electron diffraction pattern (inset) of AlB₂-type BNSLs self-assembled from 9.7 nm oleylamine-stabilized Au NCs and 17.1 nm Fe₃O₄ NCs. A 50x objective lens is used and the optical sampling area is 5.3 $\mu\text{m} \times 5.3 \mu\text{m}$.

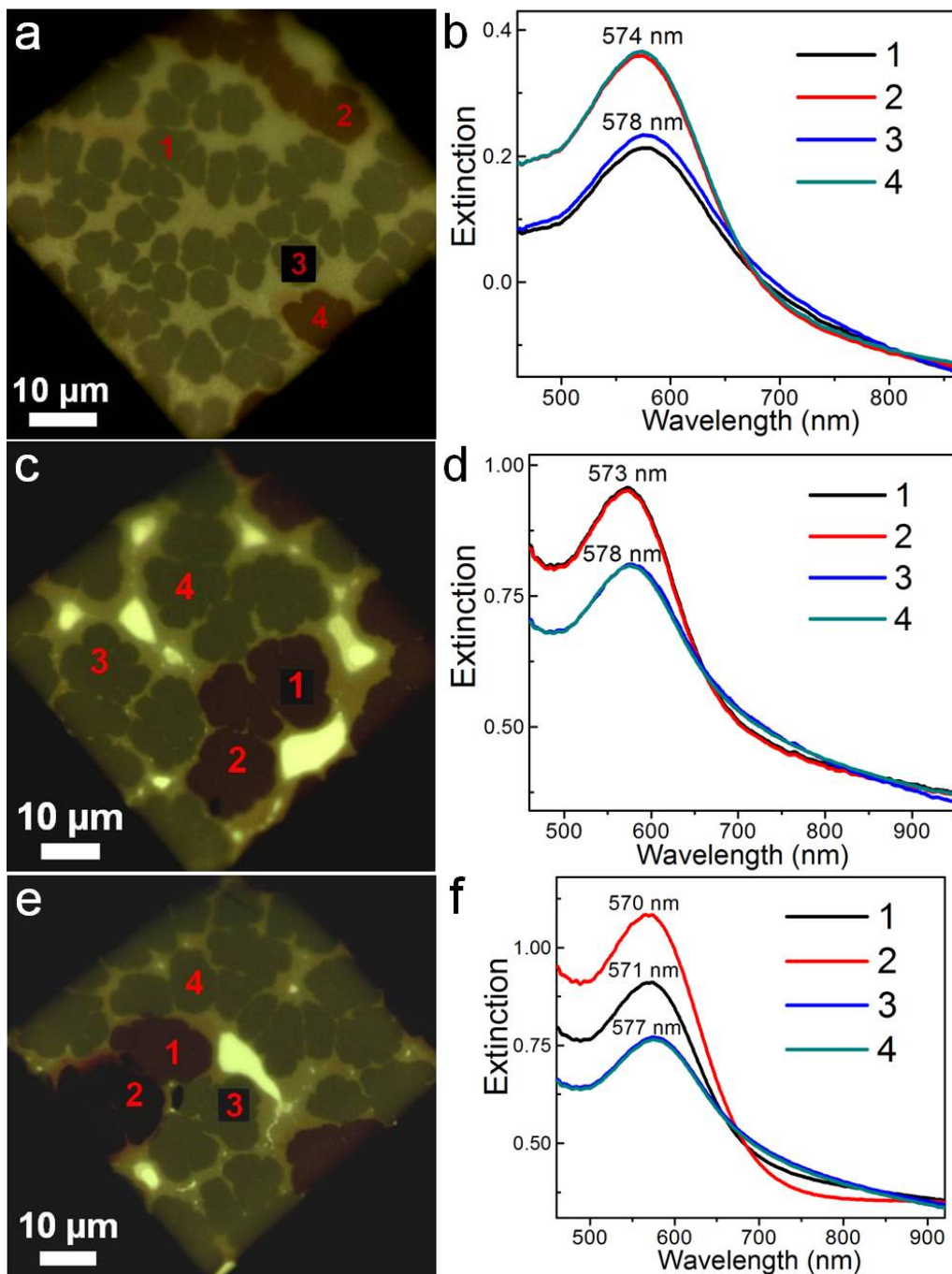


Figure S16. (a, c, e) Optical micrographs of AlB₂-type BNSLs self-assembled from 9.7 nm oleylamine-stabilized Au NCs and 17.1 nm Fe₃O₄ NCs. (b, d, f) Extinction spectra collected from different single-crystalline BNSL domains as labelled in the corresponding optical micrographs. A 50x objective lens is used and the optical sampling area is 5.3 μm x 5.3 μm.

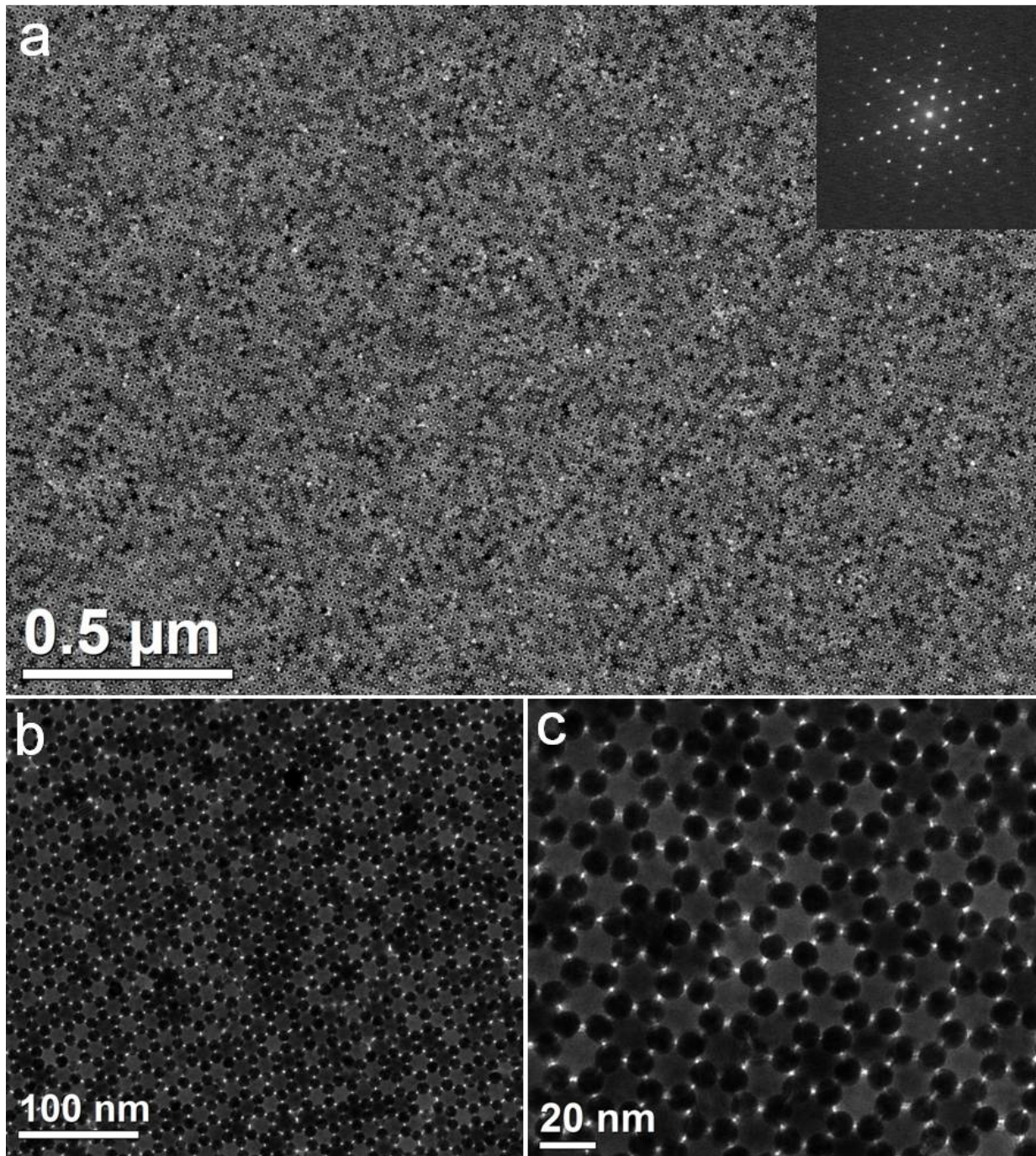


Figure S17. (a) Low-magnification and (b, c) high-magnification TEM images of AlB₂-type BNSLs self-assembled from 9.7 nm oleylamine-stabilized Au NCs and 17.1 nm Fe₃O₄ NCs. Inset of (a) shows the corresponding small-angle electron diffraction pattern.

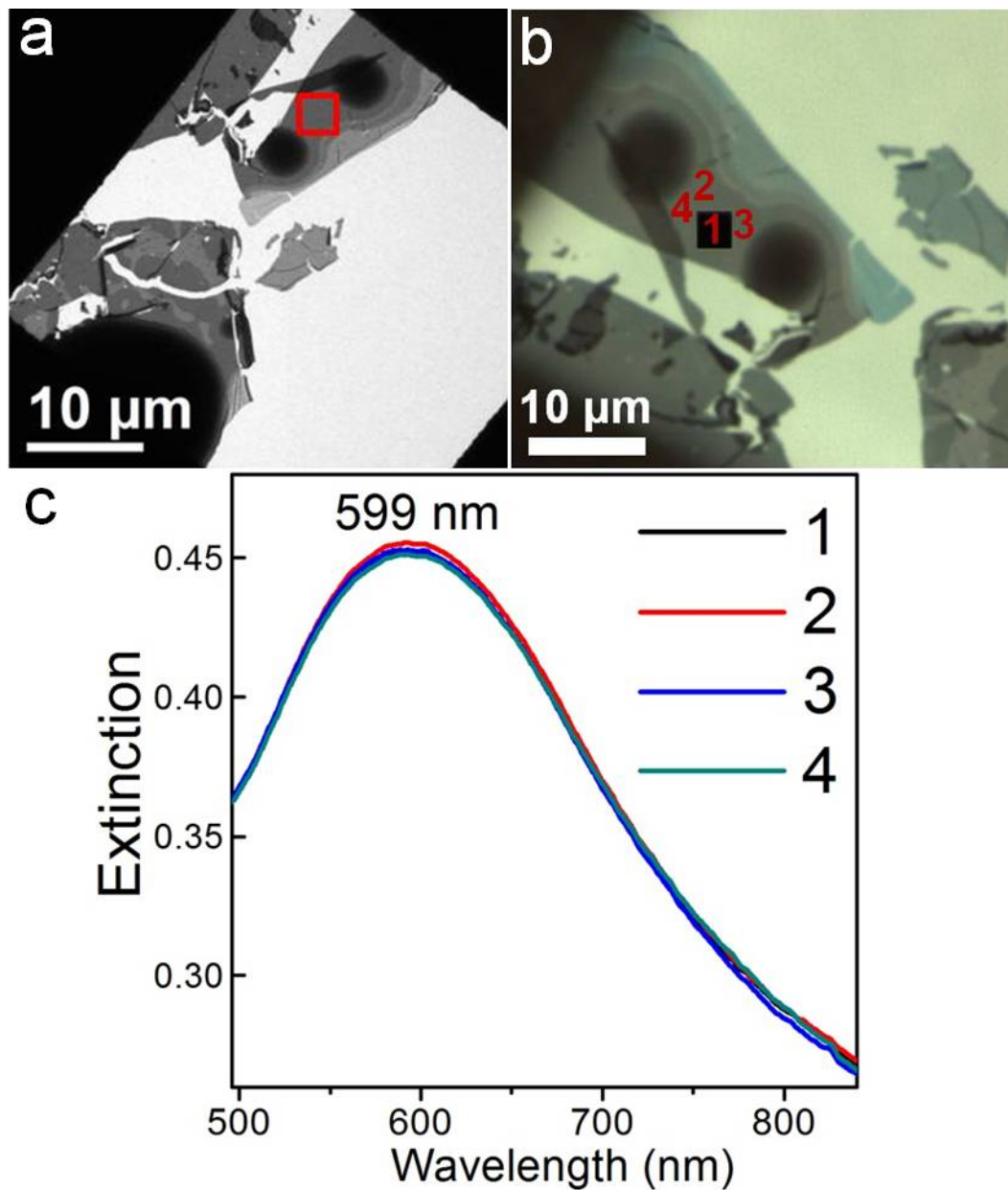


Figure S18. (a) Low-magnification TEM images and (b) corresponding optical micrographs of CaCu₅-type BNSLs self-assembled from 9.7 nm oleylamine-stabilized Au NCs and 14.1 nm Fe₃O₄ NCs. (c) Extinction spectra collected from different single-crystalline BNSL domains as labelled in the corresponding optical micrographs. A 100x objective lens is used and the optical sampling area is 3.1 μm x 3.1 μm .

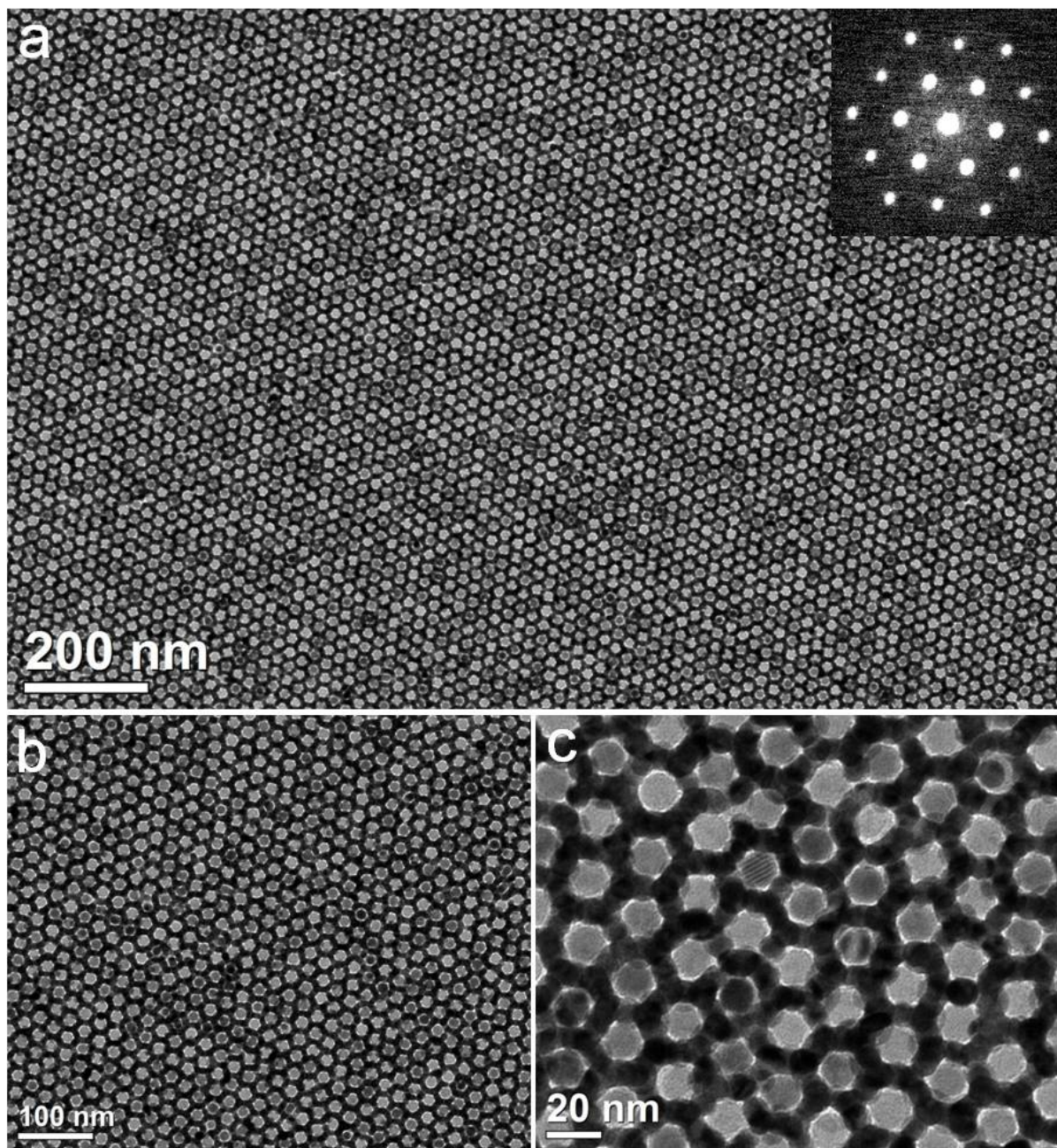


Figure S19. (a) Low-magnification and (b, c) high-magnification TEM images of CaCu₅-type BNSLs self-assembled from 9.7 nm oleylamine-stabilized Au NCs and 14.1 nm Fe₃O₄ NCs. Inset of (a) shows the corresponding small-angle electron diffraction pattern.

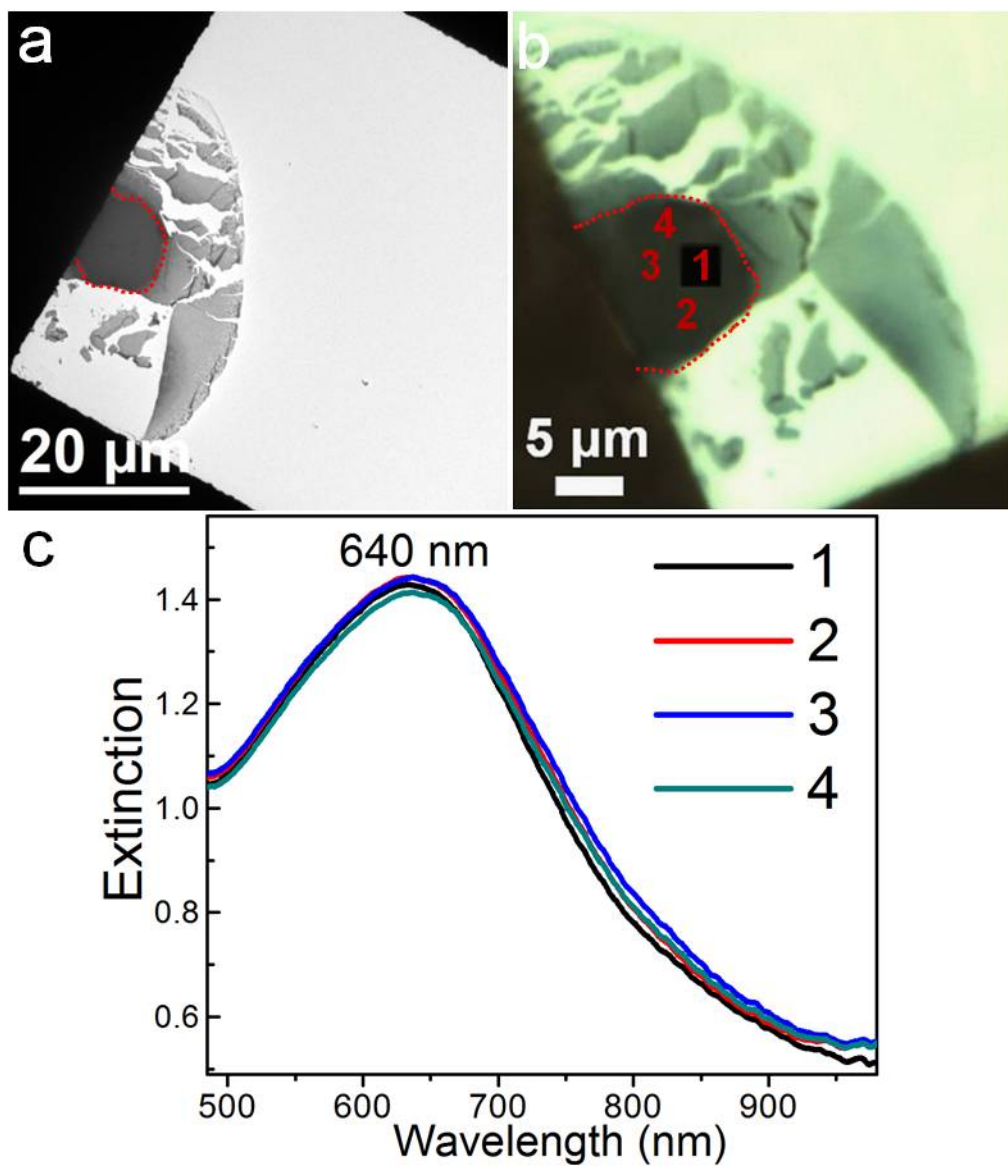


Figure S20. (a) Low-magnification TEM images and (b) corresponding optical micrographs of NaZn₁₃-type BNSLs self-assembled from 9.7 nm oleylamine-stabilized Au NCs and 17.1 nm Fe₃O₄ NCs. (c) Extinction spectra collected from different single-crystalline BNSL domains as labelled in the corresponding optical micrographs. A 100x objective lens is used and the optical sampling area is 3.1 μm x 3.1 μm.

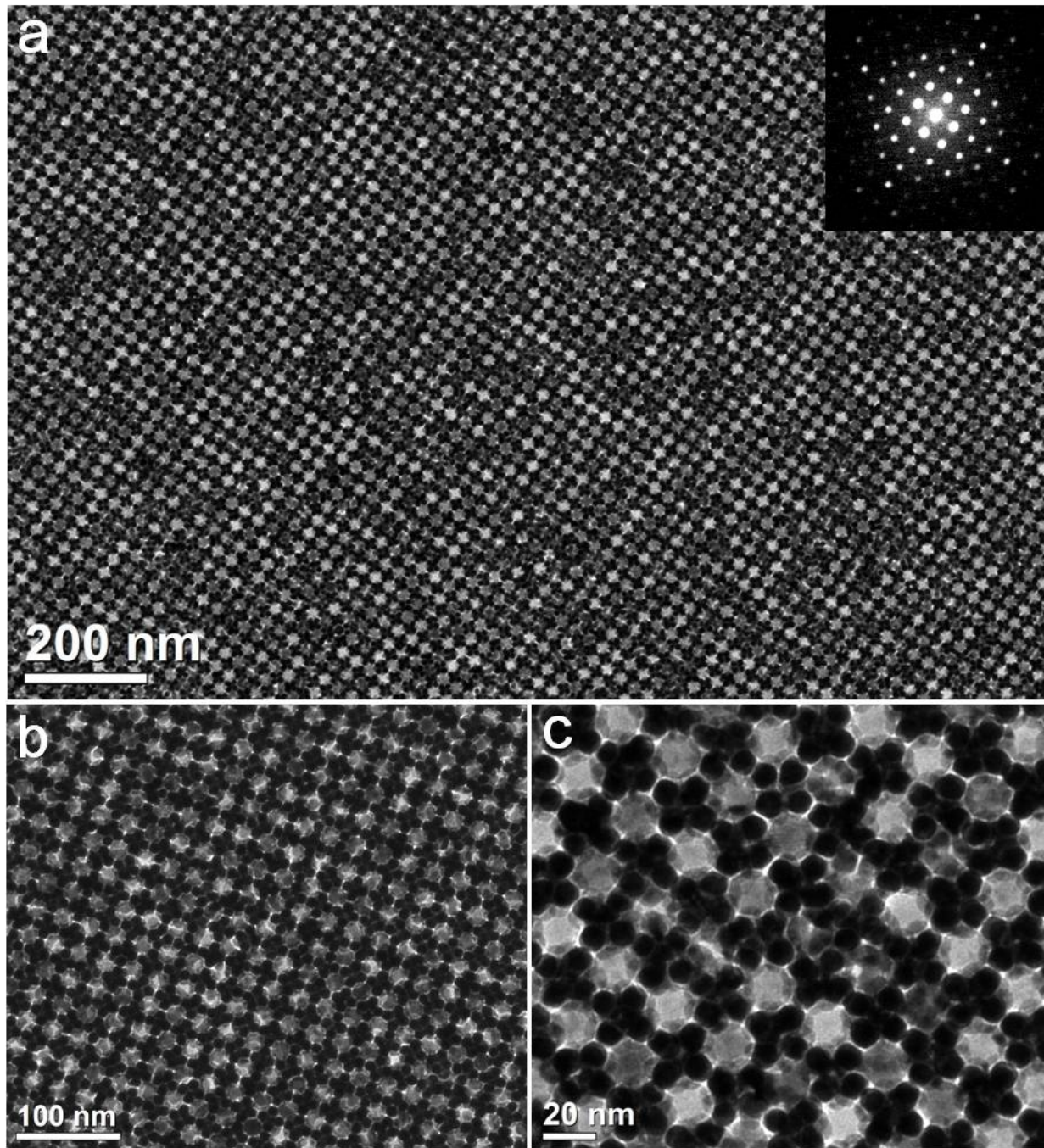


Figure S21. (a) Low-magnification and (b, c) high-magnification TEM images of NaZn₁₃-type BNSLs self-assembled from 9.7 nm oleylamine-stabilized Au NCs and 17.1 nm Fe₃O₄ NCs. Inset of (a) shows the corresponding small-angle electron diffraction pattern.

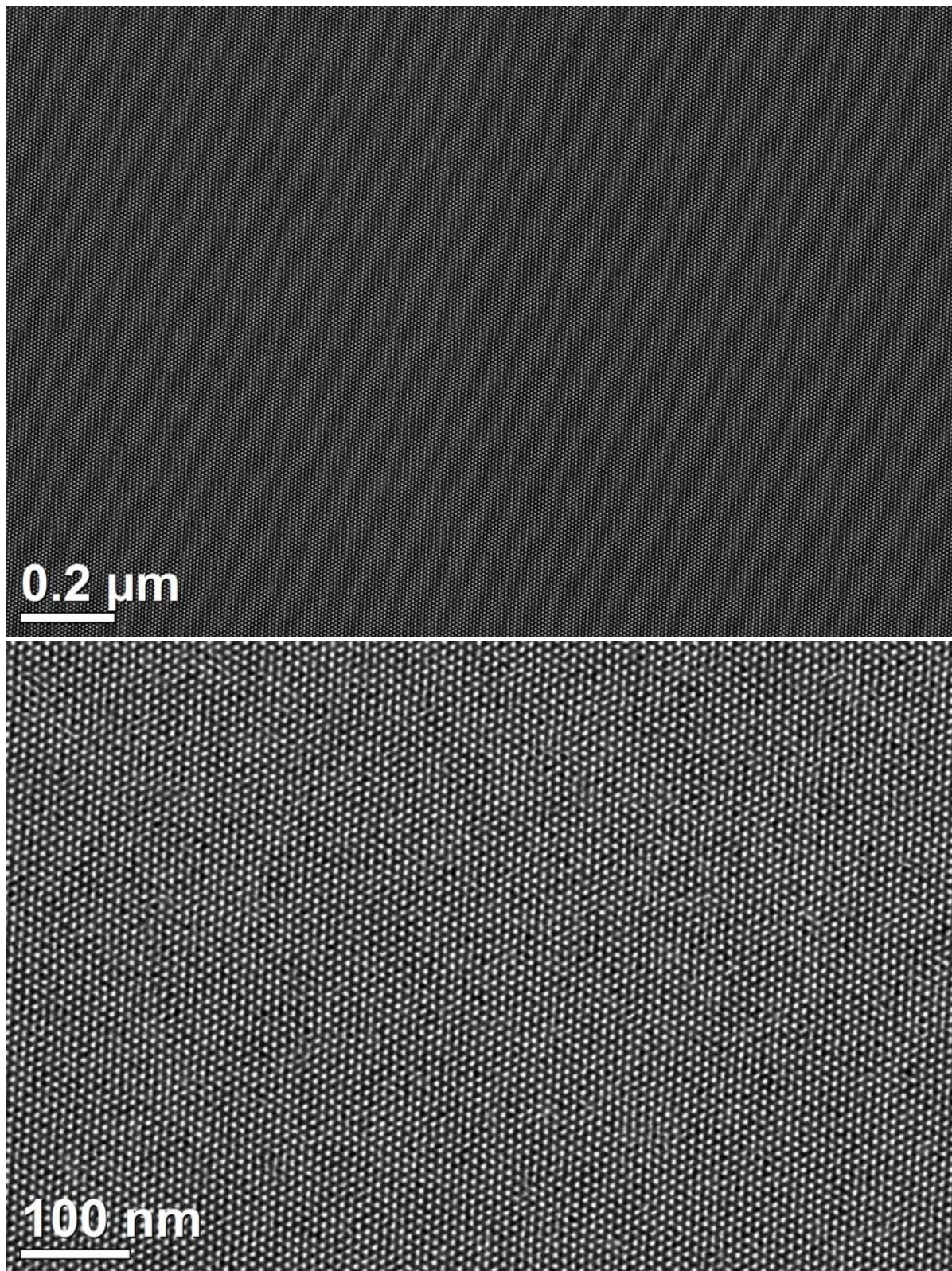


Figure S22. TEM images of hcp superlattices (three layers thick) of 5.4 nm dodecanethiol-stabilized Ag NCs.

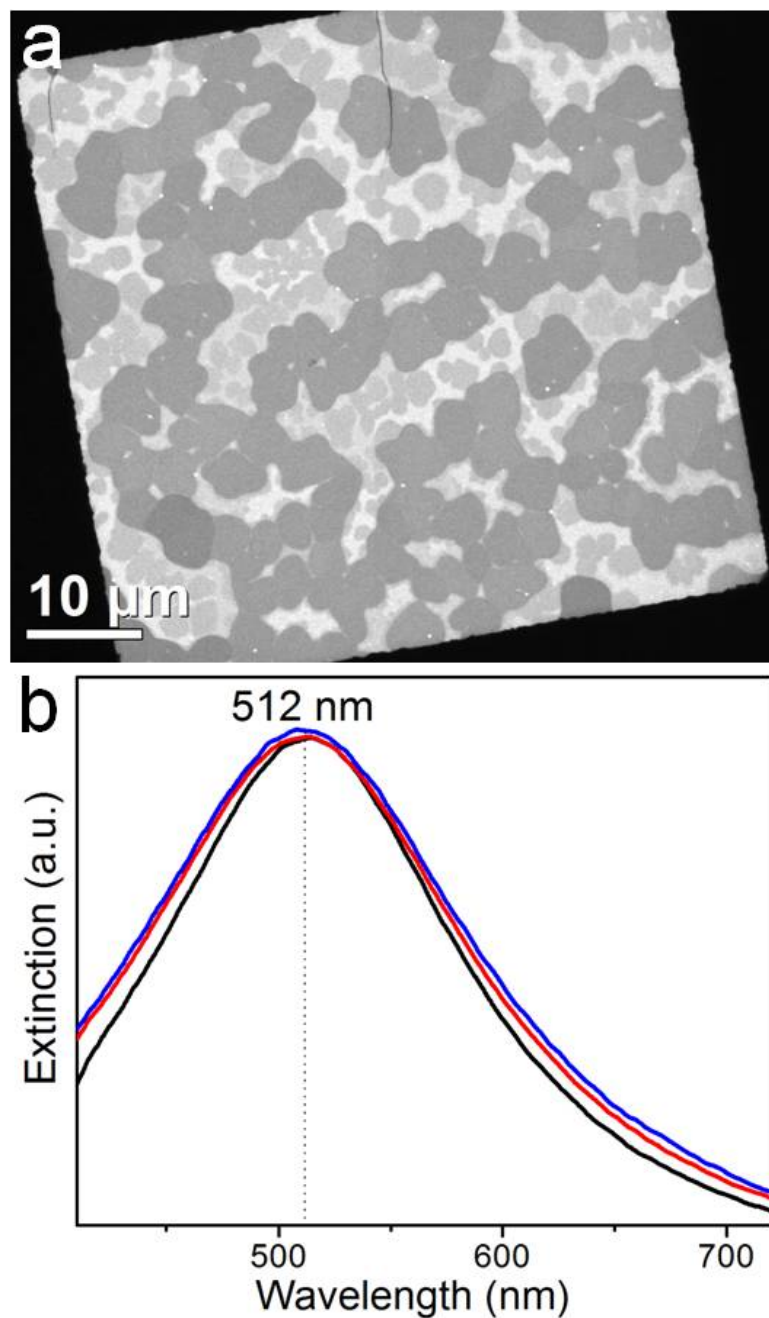


Figure S23. (a) Low-magnification TEM image of self-assembled hcp superlattices of 5.4 nm dodecanethiol-stabilized Ag NCs. Most of the darker domains are confirmed by high-magnification TEM to be three layers thick while those lighter domains are either bilayers or regions that are sparsely covered by Ag NCs. (b) Extinction spectra collected from three different hcp superlattice domains (three layers thick) of 5.4 nm dodecanethiol-stabilized Ag NCs. A 50x objective lens is used and the optical sampling area is 5.3 $\mu\text{m} \times 5.3 \mu\text{m}$.

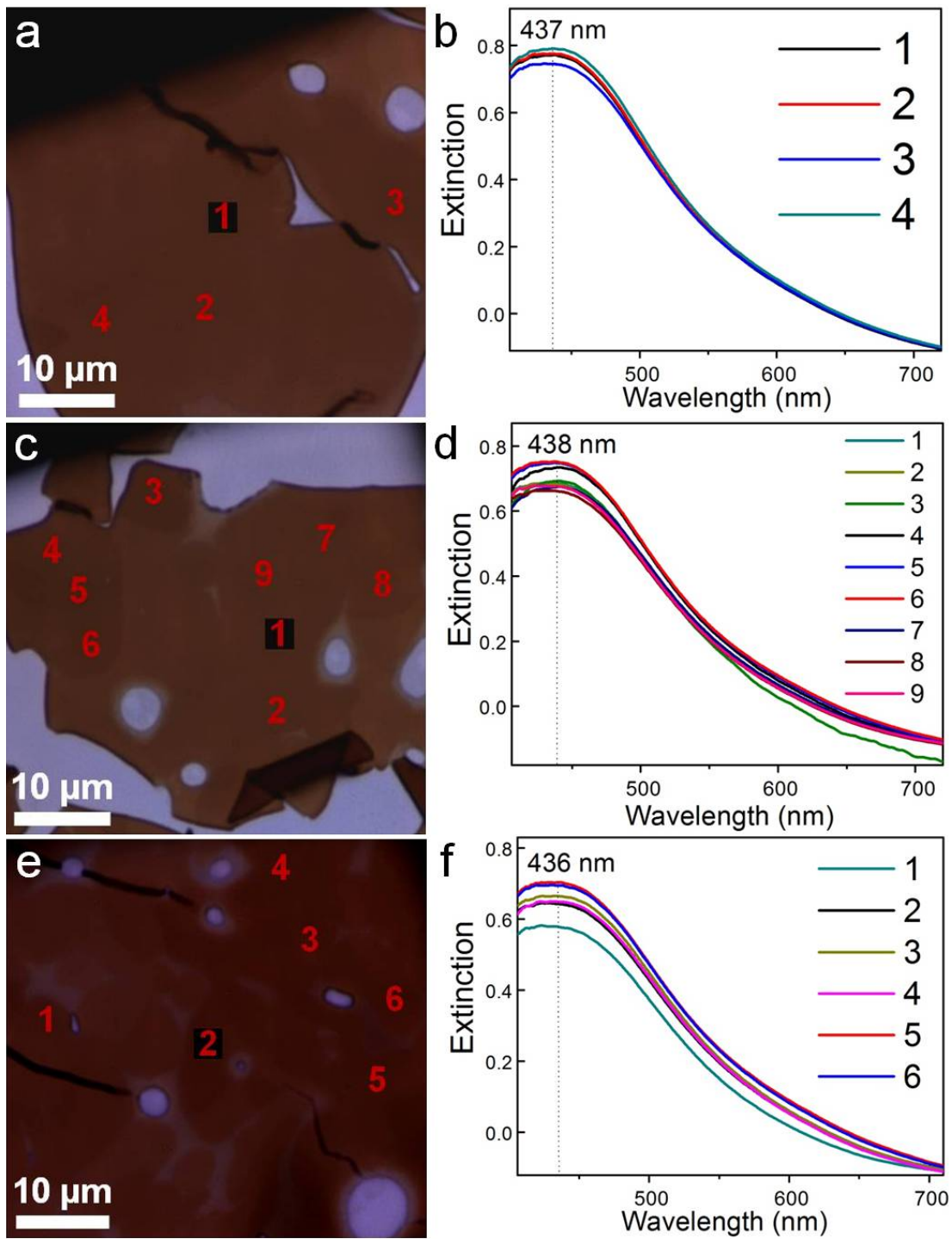


Figure S24. (a, c, e) Optical micrographs of CsCl-type BNSLs self-assembled from 5.4 nm dodecanethiol-stabilized Ag NCs and 9.3 nm PbS NCs. (b, d, f) Extinction spectra collected from different single-crystalline BNSL domains as labelled in the corresponding optical micrographs. A 100x objective lens is used and the optical sampling area is 3.1 μm x 3.1 μm.

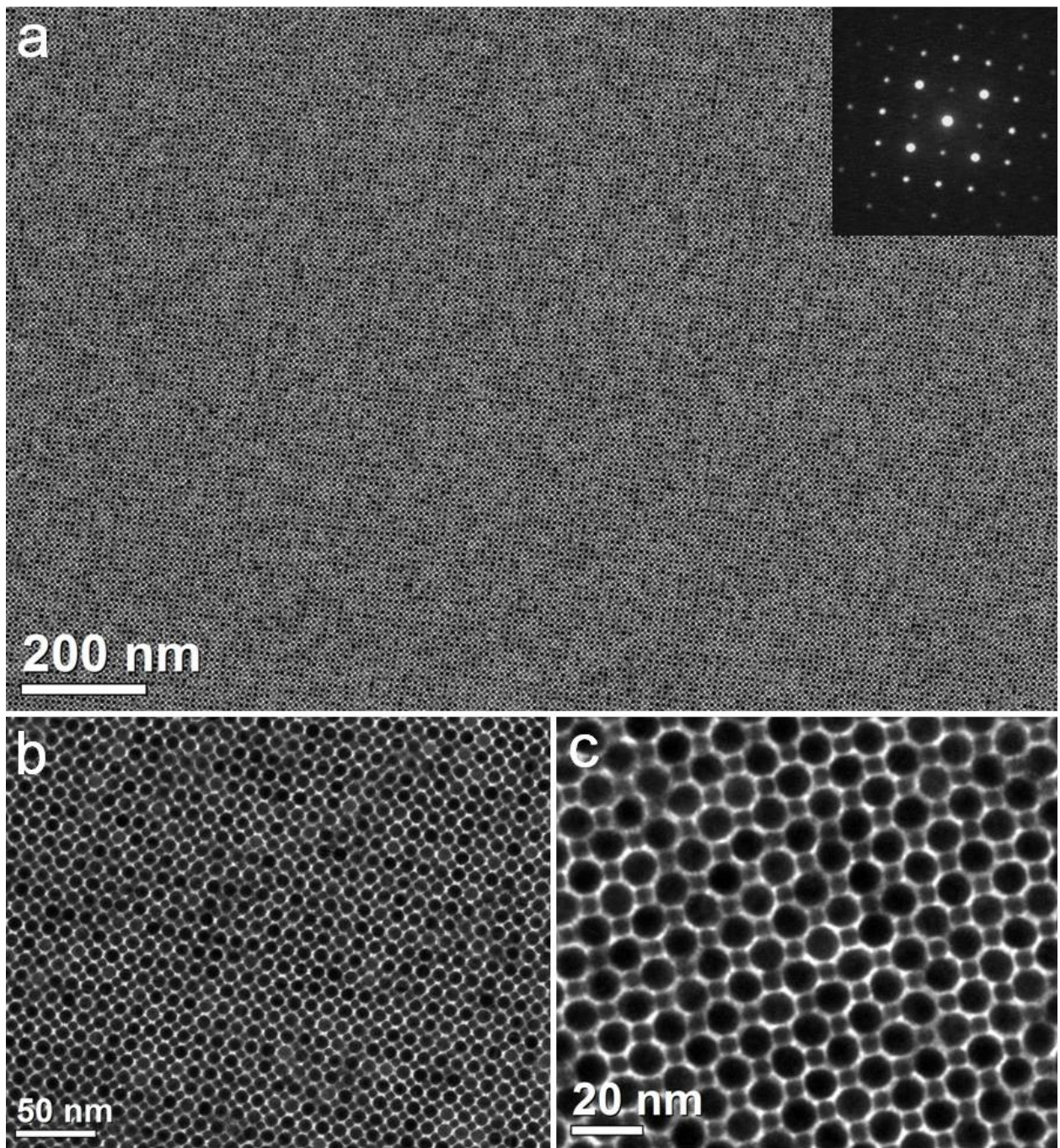


Figure S25. (a) Low-magnification and (b, c) high-magnification TEM images of CsCl-type BNSLs self-assembled from 5.4 nm dodecanethiol-stabilized Ag NCs and 9.3 nm PbS NCs. Inset of (a) shows the corresponding small-angle electron diffraction pattern.

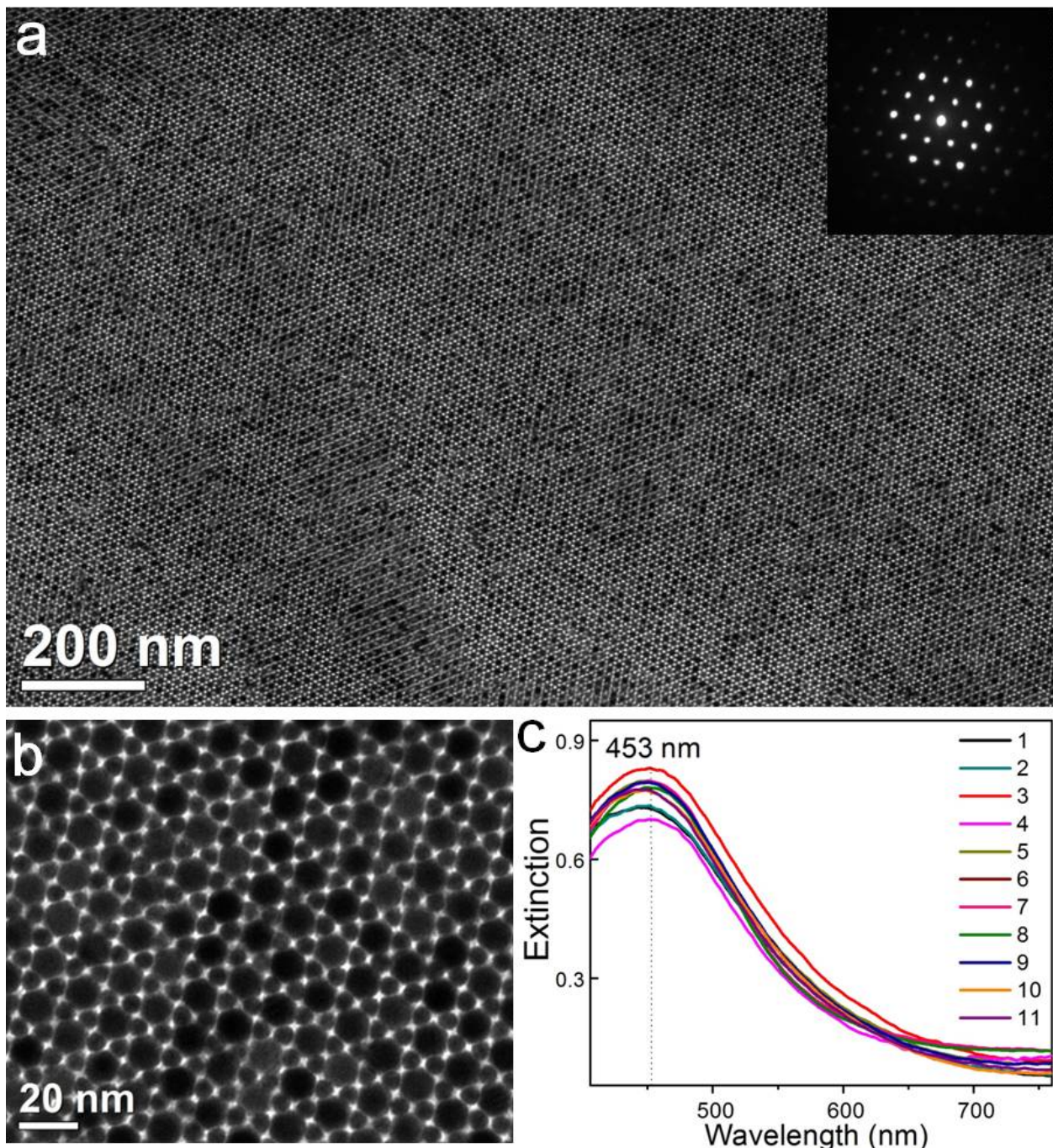


Figure S26. (a) Low-magnification and (b) high-magnification TEM images of AlB₂-type BNSLs self-assembled from 5.4 nm dodecanethiol-stabilized Ag NCs and 9.3 nm PbS NCs. Inset of (a) shows the corresponding small-angle electron diffraction pattern. (c) Extinction spectra collected from eleven different AlB₂-type Ag-PbS BNSL domains. A 100x objective lens is used and the optical sampling area is 3.1 μm x 3.1 μm .

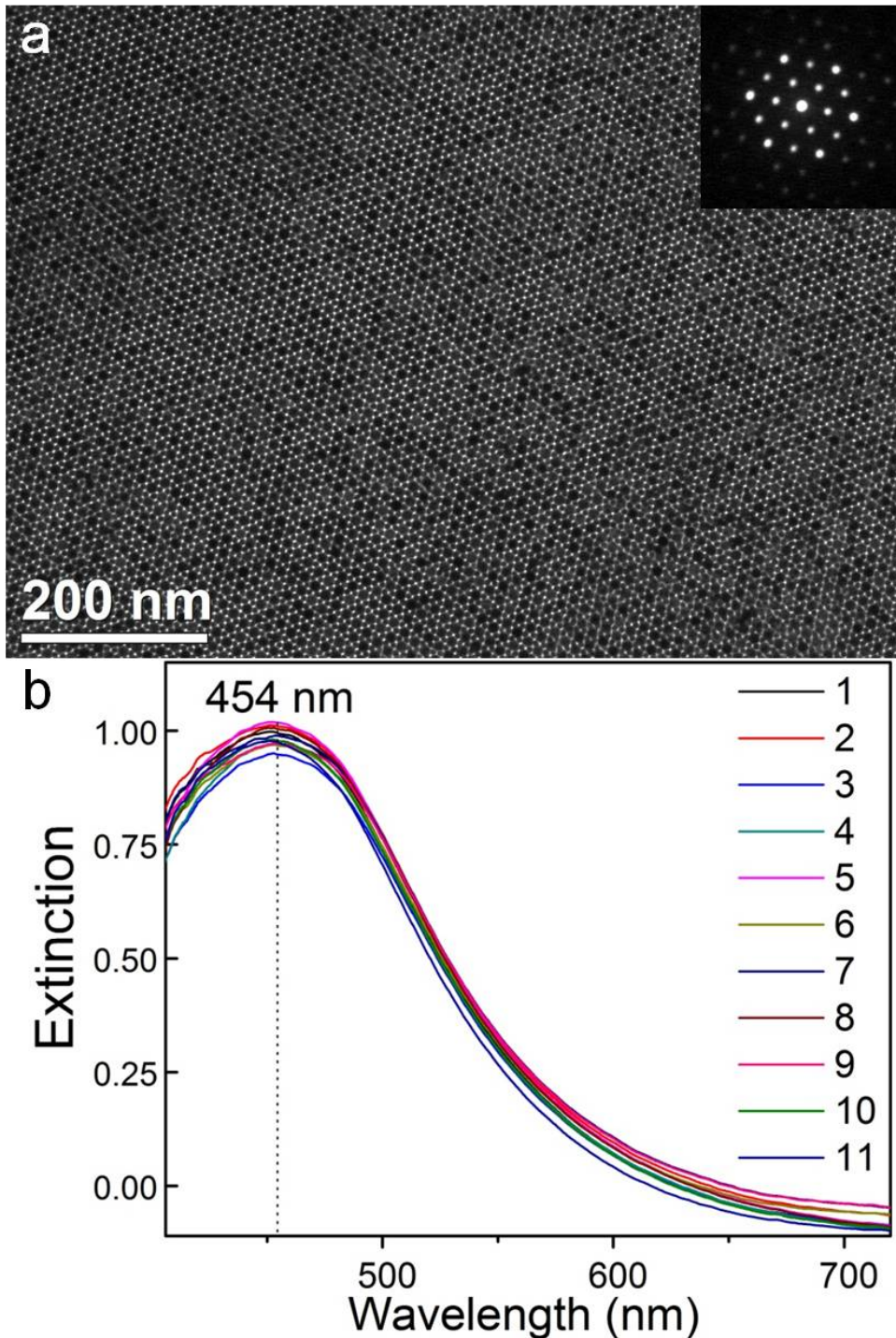


Figure S27. (a) TEM image of AlB₂-type BNSLs self-assembled from 5.4 nm dodecanethiol-stabilized Ag NCs and 9.6 nm Fe₃O₄ NCs. Inset of (a) shows the corresponding small-angle electron diffraction pattern. (b) Extinction spectra collected from eleven different AlB₂-type Ag-Fe₃O₄ BNSL domains. A 100x objective lens is used and the optical sampling area is 3.1 μm x 3.1 μm .

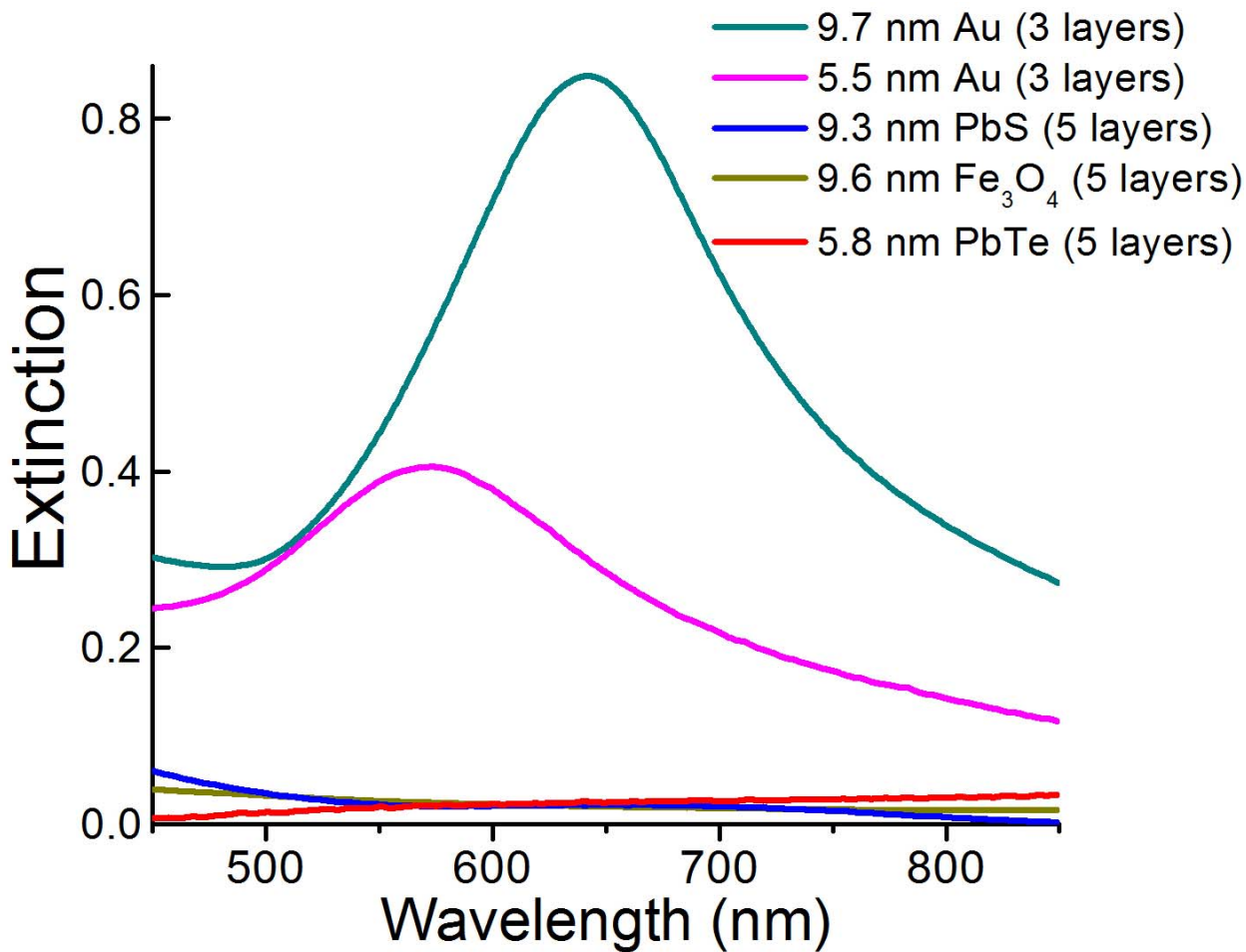


Figure S28. Extinction spectra of hcp single-component nanocrystal superlattice. The number of nanocrystal layers of the measured superlattice domains is indicated in the graph. A 50x objective lens is used and the optical sampling area is $5.3 \mu\text{m} \times 5.3 \mu\text{m}$. The non-metal nanocrystals (PbS, PbTe and Fe_3O_4) have a much smaller molar extinction coefficients compared to similar sized Au nanocrystals in the blue-green spectral region, and none of them show distinct absorption peaks in the visible range. Therefore, we believe that the optical response of the non-metal nanocrystals or the coupling between metal and these non-metal nanocrystals do not play an important role in determining the collective plasmonic response of BNSLs.

References

- S1. Hines, M. A.; Scholes, G. D. *Adv. Mater.* **2003**, *15*, 1844-1849.
- S2. Urban, J. J.; Talapin, D. V.; Shevchenko, E. V.; Murray, C. B. *J. Am. Chem. Soc.* **2006**, *128*, 3248-3255.
- S3. Park, J.; An, K. J.; Hwang, Y. S.; Park, J. G.; Noh, H. J.; Kim, J. Y.; Park, J. H.; Hwang, N. M.; Hyeon, T. *Nat. Mater.* **2004**, *3*, 891-895.
- S4. Ye, X.; Chen, J.; Murray, C. B. *J. Am. Chem. Soc.* **2011**, *133*, 2613-2620.
- S5. Shen, C.; Hui, C.; Yang, T.; Xiao, C.; Tian, J.; Bao, L.; Chen, S.; Ding, H.; Gao, H. *Chem. Mater.* **2008**, *20*, 6939-6944.